Reviewer comments on 'Influence of low-level blocking and turbulence on the microphysics of a mixed-phase cloud in an inner-Alpine valley' by Fabiola Ramelli et al.

Response to Dmitri Moisseev

We would like to thank Dmitri Moisseev for his constructive and helpful feedback and suggestions on the manuscript. We incorporated the suggestions within the revised manuscript, which significantly improved the quality of the manuscript. In the following, we will address the reviewer's comments and present our responses and changes in the revised manuscript. Reviewer comments are reproduced in blue and author responses are in black. All line numbers in the author's response refer to the revised manuscript.

General comments

1) *The authors investigate the influence of low-level blocking and shear induced turbulence on the cloud microphysics. They find associated changes in the cloud microphysics associated. Additionally, a low-level feeder cloud is observed and seems to be caused by the low-level blocking. This study is of great interest and importance for our understanding of the cloud processes in mountainous regions. I believe this paper can be published after major revisions. I am not sure if I completely agree with the authors' interpretation of radar observations and would like to see more explanations and answers to my questions. Please find my comments below.*

   Thank you for your comments and for raising several points, which in particular improved the interpretation of the radar observations. We included riming and the Hallett-Mossop process as possible microphysical mechanisms active within the mid-level cloud. The interpretation and discussion of the case study changed accordingly, as addressed in the responses to the specific comments.

Specific comments

2) *Lines 157-162. The interpretation of LDR (or any other dual-polarization radar variable) is a bit more complex. It is true that LDR depends on an apparent shape of a hydrometeor. However, to make matters more complex, it also depends on the particle refractive index, in case of ice particles the refractive index is related to the particle density. Therefore, increase in the ice particle density, i.e. by riming, may increase LDR. That is why changes in LDR are not necessary indicative of the changes in particle shape (see for example Fig. 2.8 page 65 in (Bringi and Chandrasekar, 2001)).*

   Another example is the change of LDR in the melting layer of precipitation, it is driven by the changes in the refractive index due to melting and not changes in particle shape.

   Thank you for this comment and the references. Indeed, as you pointed out the LDR signal depends on both the shape and density of the hydrometeors. We have now added a short description about the dependence of the LDR on the particle refractive index and included the proposed references (page 7, line 166-169): *"Furthermore, the LDR depends on the particle refractive index. Liquid water has a higher refractive index (0.93) than ice (0.197) (Houze Jr, 2014). For ice particles, the refractive index is related to the particle density, such that hail and graupel have a higher refractive index compared to snowflakes (Bringi and Chandrasekar, 2001). Therefore, changes in the LDR are indicative for changes in the particle shape and/or particle density (e.g. riming)."*

3) *Line 237. "an increase in the LDR was observed within the shear layer (Fig. 8e, f), which is indicative of a change in the hydrometeor shape" Actually, to my eye the increase in LDR starts above the shear layer. It may be related to the increase in Doppler velocity as shown in Fig. 10. Such an increase in Doppler velocity may be indicative of riming (Mosimann, 1995; Kneifel and Moisseev, 2020), which affects LDR as well.*

Thank you for this comment and the references. We agree that the increase in the Doppler velocity might be related to riming. Especially, since the LDR of the faster falling part of the spectrum was observed to increase (Fig. 10). As no in situ observations were available within the upper part of the shear layer, we cannot draw any conclusions regarding the dominant microphysical processes. Thus, we discuss both riming and aggregation as possible ice growth mechanisms within the shear layer. We extended the interpretation as follows and included the suggested references (page 14, line 267-274):*" The increase in the Doppler velocity might be indicative of riming. Previous studies observed that an increase in the Doppler velocity can be indicative of riming, which leads to a higher terminal fall velocity of particles due to the rapid gain of ice particle mass (e.g., Mosimann, 1995; Kneifel and Moisseev, 2020). This is further supported by the increase in the LDR of the faster falling population of the spectrum as a consequence of the higher particle density. In addition, turbulence within the shear layer could increase the number of collisions between ice particles and promote the formation of aggregated particles (e.g., Pinsky and Khain, 1998)."*

4) *Line 248-249: "This is in agreement … with the ice particles observed by the MASC at the surface (Fig. 11a)." Actually, MASC observations do show presence of rimed particles as well.*

Thank you for pointing this out. We changed the sentence as follows (page 16, line 273-274): *"Indeed, the hydrometeors observed by the MASC and HOLIMO show indications of rimed particles and large aggregates (Fig. 11), suggesting that both processes were occurring."*

5) *Line 250: "Below 3000 m, the LDR increased up to -20 dB within the fallstreak (Fig. 10b)." It is not clear what you are referring to. Please indicate on the spectra which part has LDR values up to -20 dB.*

If this is the faster falling part of the spectrum, then it cannot be due to newly formed ice crystals. In this case, in my opinion it would be riming. If the increase in LDR occurs in the slow falling part then it is cause by newly formed ice particles.

Thank you for this comment. We specified in which part of the spectra the LDR increased (page 14, line 262-264): *"Below 3000 m, the LDR of the faster falling part of the spectrum increased up to -21 dB (Fig. 10b) and the spectrum broadened (Fig.10a)."* As you pointed out correctly, this suggests that the increase in the LDR was due to riming on the faster falling particles, which then led to the increase in the Doppler velocity. Accordingly, the interpretation of the LDR signal was changed (page 14, line 267-271): "*The increase in the Doppler velocity might be indicative of riming. Previous studies observed that an increase in the Doppler velocity can be indicative of riming, which leads to a higher terminal fall velocity of particles due to the rapid gain of ice particle mass (e.g., Mosimann, 1995; Kneifel and Moisseev, 2020). This is further supported by the increase in the LDR of the faster falling population of the spectrum as a consequence of the higher particle density."*

6) *Line 254: "An increase in the LDR can be explained by the presence of needles, columns and/or irregular ice particles."*

Do you observe this in Doppler spectra? You should see bimodal spectra, or at least some indication of bimodality.

Thank you for this comment. The Doppler spectra shows no indications of bimodalities, which would support the formation of a newly formed particle population. However, possible bimodalities might be masked by turbulence or subsaturated regions. The particles observed by HOLIMO show indications of needle growth on existing ice particles. We changed the text as follows (page 16, line 283-286): *"The analysis of the Doppler spectra showed no evidence of discrete multiple spectral peaks (i.e., the presence of multiple particle populations with different fall speed), which would support the occurrence of secondary ice production. However, turbulent regions or sublimation could broaden the size distributions and thus mask the presence of discrete multiple peaks in the Doppler spectra."*

7) *Line 259 – 261: "If fragile ice crystals such as dendrites or needle-like structures collide with large ice particles within the turbulent shear layer, small ice fragments might break off and lead to the production of secondary ice particles upon collision (e.g., Vardiman, 1978; Yano et al., 2016)."*

   Of course, it may also be H-M process if the LDR signatures caused by riming.

   Thank you for this comment. Indeed, the temperature (-8 °C to -4 °C) was in the temperature range of the Hallett-Mossop process. Thus, it is possible that secondary ice particles were produced upon riming. We added a sentence describing the possible occurrence of the Hallett-Mossop process (page 16, line 275-277): *"The temperature between 3000m and 2500m ranged from -8 °C to -4 °C and was thus in the temperature regime of columnar growth and of the Hallett-Mossop process. Thus, secondary ice particles might be produced upon riming, which could then rapidly grow by vapor deposition into column-like particles."* We also state that due to the missing in situ observations within the upper part of the shear layer it was not possible to draw any conclusions regarding the occurrence of secondary ice mechanisms (page 17, line 290-292): *"It remains unclear whether the Hallett-Mossop process and mechanical break-up in ice-ice collisions contributed to the formation of secondary ice particles (see also Sect. 5)."*

8) *Line 326-327: "Riming was assumed to play only a minor role, due to the low LWP (< 100 g m−2) observed by the microwave radiometer (Fig. 4c)." I am not sure if I agree that we can completely exclude riming based on LWP alone. Riming efficiency does not depend on LWP, but on liquid droplet diameter. So, given that droplets are big enough to take part in riming, riming could take place. We can compute if riming would significantly affect particle properties, by computing rime mass fraction for the observed LWP values. Let's assume that we a plate like crystal is formed at the cloud top. Just to have a first guess, we can choose P1a from Pruppacher and Klett.*

TABLE 2.4a

Mass-size relationships for various types snow crystals. Data taken on Mt. Teine (1024 m, Hokkaido, Japan), based on data of Heymsfield & Kajikawa, 1987.

Crystal type	Mass-size relation m(g), d(cm)	Diameter range (mm)
C1h	$2.63 \times 10^{-2}\ d^{2.68}$	0.3-0.6
P1a	$3.76 \times 10^{-2}\ d^{3.31}$	0.3-1.5

We can compute the expected FR as (see my simple Matlab code):

```
d = 0.3:0.01:1.5; %% mm
m = 3.76 * (10^-2) .* ((d/10).^3.31); %% grams for P1a

LWP = 50; % g/m^2


dm  = LWP.*(pi/4).* (d/100).^2;

%%% Rime mass fraction
FR = dm./(m+dm);
```

This computation gives rime mass fraction value close to 1. Of course, I have assumed the riming efficiency of 1, here. So, the actual FR value could be lower. But notice that I have used LWP of 50 g/m^2 and not 100 g/m^2.

If riming is taking place here, even for the observed low LWP values we can expect a significant impact on particle properties.

Thank you for the comment and the calculation. The calculation clearly shows that riming cannot be excluded based on the LWP alone. Based on your previous comments (see also answers to comments #2 to #4), we included riming as a possible ice growth mechanism in the revised manuscript (especially due to the increase in the negative Doppler velocity and the increase in the LDR of the faster falling population of the spectrum). Furthermore, the ice particles observed by the MASC and HOLIMO show indications of riming. We also discuss the possible role of the Hallett-Mossop process in the revised manuscript (see answer to comment #7).

Reviewer comments on 'Influence of low-level blocking and turbulence on the microphysics of a mixed-phase cloud in an inner-Alpine valley' by Fabiola Ramelli et al.

Response to Reviewer #2

We would like to thank the anonymous referee for his/her constructive and helpful feedback and suggestions on the manuscript. We incorporated the suggestions within the revised manuscript, which significantly improved the quality of the manuscript. In the following, we will address the reviewer's comments and present our responses and changes in the revised manuscript. Reviewer comments are reproduced in blue and the author responses are in black. All line numbers in the author's response refer to the revised manuscript.

General comments

1) *This manuscript uses a wide variety of ground-based observations to investigate the impact that orography can have on cloud microphysics in an Alpine environment. Understanding this impact is obviously important for increasing the accuracy of weather and climate forecasts in orographic regions, and the applications that depend on these forecasts.*

   According to the title, the major objective is to examine the effect of low-level blocking and turbulence on mixed-phase cloud microphysics, and a conceptual figure is given and discussed. The scope of the manuscript is rather broad, and tries to cover too many aspects without enough attention to detail. Many possible processes are described but, often, not enough evidence is presented in interpreting the observations. To be published, this manuscript requires major revisions. In my opinion, the manuscript would benefit from a much tighter focus, and a discussion reduced to the relevant processes backed by evidence. A major issue is that low-level blocking and wind shear are not likely to be having an impact on the formation of the mixed-phase cloud (the supercooled liquid layer at cloud top) but possibly modifying the precipitation as it falls, i.e. through seeder-feeder processes.

   Thank you for your comment and for raising several points, which helped to make the manuscript clearer. In particular, we shortened Section 4.2 and tried to focus on the relevant processes. It is difficult to provide conclusive evidence, as no in situ observations were available within the mid-level cloud and thus the analysis was based on remote sensing and ground-based ice particle observations. Furthermore, we removed Appendix B (correlation calculations) from the revised manuscript. On the other hand, following your suggestion, we extended Section 4.3 and investigated the reason for the formation of the low-level feeder cloud by relating the updraft velocity to the in situ measurements of the cloud properties.

   We agree that the low-level blocking and wind shear were not having an impact on the formation of the mid-level mixed-phase cloud or the supercooled liquid layer at cloud top; but that the shear layer likely modified the falling hydrometeors (e.g., through depositional growth, riming or aggregation) by providing an ice supersaturated environment. We modified some sentences in the revised manuscript to make this point clearer (see responses to specific comments). Additionally, we clarified that the blocked low-level flow was only responsible for the formation of the low-level feeder cloud (see Sect. 4.3).

Specific comments and questions

2) *This case study observes the passage of a synoptic-scale frontal system, and some of the features described in the manuscript can be directly attributed to the large scale motion rather than the orography. The sloping shear feature above 2.5 km in Figure 5 is common to many synoptic scale frontal systems (e.g. Keyser and Shapiro, 1986), and similar wind and shear patterns are often seen in weather radar, radar windprofiler or scanning cloud radars in fronts passing over much flatter, homogeneous terrain. The vertical wind shear values are also similar to those observed in fronts over more homogeneous terrain (Chapman and Browning, 2001).*

Thank you for this comment and the references. As described in Section 3.1 the case study was measured in a post-frontal environment on 7 March 2019 between 16 UTC and 20 UTC. The cold front passed the measurement site in Davos at around 8 UTC (see figure of the radar reflectivity below). We included a map of reanalysis data at 700 hPa height in the revised manuscript (see Fig. 2a) to give a better overview of the synoptic situation and extended the discussion of the synoptic situation (page 6, line 138-145): *"The synoptic situation over Europe was dominated by an occluding low-pressure system (980 hPa) located east of the British Isles. As the low-pressure system continued to propagate towards Scandinavia, it drove a cold front over the Alps, which passed the measurement location at 8 UTC. Based on observations, rainfall of up to 50 mm was produced on the southern side of the Alps during the passage of the cold front (not shown). By 15 UTC, southwesterly flow in the post-frontal air mass continued to advect cold air and moisture into the Alpine region (see Fig. 2a), which produced light precipitation on the south side of the Alps with some spillover precipitation on the lee side (i.e. north side) of the Alps. The case study was measured in the post-frontal air mass between 16 UTC and 20 UTC, when some spillover precipitation reached the measurement locations in the Davos region."*

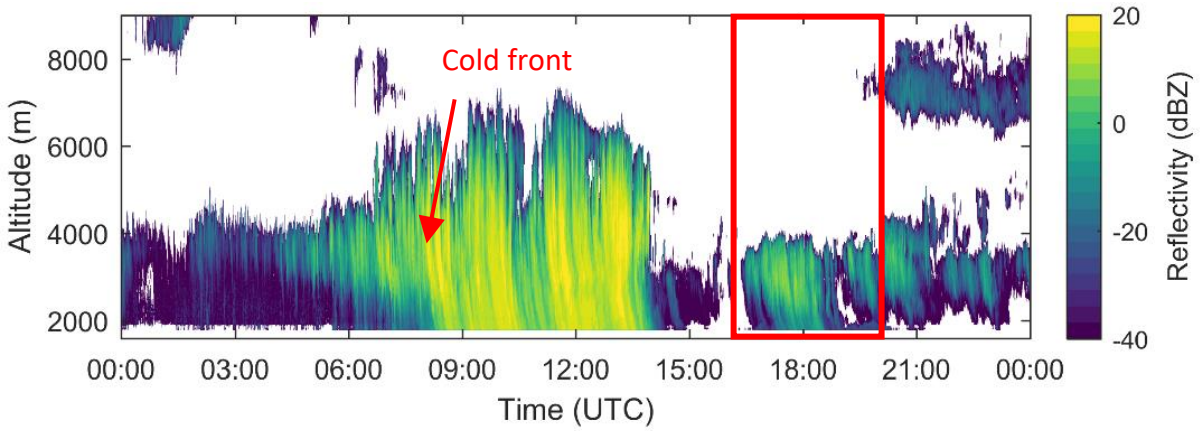

Figure 1: Radar reflectivity on 7 March 2019. The red rectangle indicates the measurement period of the present case study.

Since the synoptic frontal system passed the measurement location already in the morning, we assume that the sloping shear feature was related to the orography. This is further supported by the height of the shear layer, which was related to the altitude of the upstream mountain barrier. Since we cannot exclude an influence of the synoptic system, we extended the paragraph as follows (page 13, line 226-232): *"Sloping shear features have also been observed in connection with synoptic scale*

frontal systems (e.g. Keyser and Shapiro, 1986; Chapman and Browning, 2001), where similar vertical wind shear values have been measured (Chapman and Browning, 2001). The presented observations cannot provide conclusive evidence about whether the observed wind and shear patterns were orographically or synoptically driven. We suggest that the sloping shear feature was influenced - at least to some extent - by the orography, as the height of the shear layer was related to the altitude of the upstream mountain barrier B1 and the strength of the blocking and downward propagating cross-barrier flow (Fig. 5c, d and Fig. 7)." Furthermore, we changed the subtitle of Section 4.1 from "Low-level flow blocking triggering wind shear and turbulence" to "Low-level flow blocking and wind shear" in the revised manuscript in order to avoid a clear assignment of a cause.

3) *As shown in Figure 8, the highest radar reflectivity values are expected at the upper boundary of the sublimation zone, before the falling ice particles start to sublimate and reduce in size. Figure 8 and 9 show that the sloping shear feature appears to coincide with this sublimation zone, with the location of the maximum radar reflectivity values lowering in altitude over time just above the 0.01 s-1 wind shear contour also lowering in time. This is what would be expected if the sloping shear feature indicates the frontal boundary between two air masses, one saturated, and one subsaturated. This correlation between the upper edge of the sloping shear zone and the maximum radar reflectivity values therefore suggests that the large scale forcing could be responsible in this case.*

   Hence, without additional observations, or using output from a high resolution numerical weather prediction model, it is difficult to determine whether the changes at lowlevel (blocked/unblocked flow) are responsible for any changes at upper levels.

   Thank you for this comment. We agree that the shear layer likely indicates the boundary between a saturated and a subsaturated air mass. However, we suggest that the flow separation (dry boundary layer in the valley/ moist cross-barrier flow aloft) occurs due to the upstream topography, since the synoptic scale-frontal system passed the measurement location already in the morning and the height of the shear layer was related to the altitude of the orography (see also response to previous review comment).

   The boundary between the two air masses was characterized by a turbulent shear layer. We suggest that the hydrometeors falling through the shear layer from above likely experience changes in the cloud properties as indicated by the enhanced radar reflectivity (increased ice growth) and the increase in LDR (change in particle shape or density). Thus, we agree that the low-level blocking did not directly influence the formation and microphysics of the mid-level cloud. Instead, the blocked layer influenced, in combination with the strength of the downward propagating cross-barrier flow, the altitude of the shear layer. We modified some sentences in the revised manuscript to make this point clearer (page 21, line 341-345): *"The ice particles encountered a turbulent shear layer while falling through the cloud, within which changes in the microphysical cloud properties were observed including enhanced radar reflectivity (i.e., increased ice growth) and LDR (i.e., change in particle shape or density). This suggests that the turbulent shear layer created an ice supersaturated environment and thereby influenced the cloud microphysics."*

4) *The wind shear values derived from the two instruments are not always consistent with each other. Is this due to the differences in spatial and temporal resolution, scan pattern or integration time? Please include the elevation angle that the wind profiler operates at and the scan pattern used by the Doppler*

lidar for deriving winds. The wind calculations assume a homogeneous wind field and it is known some scanning patterns are more susceptible to turbulence, which can mean that this assumption is no longer valid (Päschke et al., 2015). How much of an impact could the turbulent zones have on the horizontal wind and shear calculations? How about variations in the particle fall velocity?

Päschke, E., R. Leinweber, and V. Lehmann (2015), An assessment of the performance of a 1.5 m Doppler lidar for operational vertical wind profiling based on a 1-year trial, Atmos. Meas. Tech., 8, 2251–2266, doi:10.5194/amt-8-2251-2015.

Thank you for this comment. The differences in the vertical wind shear are mostly due to different vertical and temporal resolution of the wind profiler and wind lidar. The temporal and spatial resolution are specified on page 5, line 122-124: *"The wind profiler had a temporal resolution of 5 min and a vertical resolution of 200 m, whereas the wind lidar provided wind measurements with a higher vertical resolution of 50 m."* This pattern is also visible on Figure 5. Furthermore, we included the elevation angle and the scan pattern used by the wind lidar in the revised manuscript (page 5, line 124-126): *"The wind lidar operated in Doppler Beam Switching (DBS) mode with 4 beams at an elevation angle of 75° and a vertical beam. Additionally, Range Height Indicator scans (RHI) were performed every 30 minutes in four different azimuth directions (0°, 70°, 180° and 250°)."* The wind profiler had a vertical beam as specified on page 5, line 121 in the revised manuscript. DBS is a widely used technique to measure 3D wind properties. According to a manufacturer, both VAD and DBS can be used to retrieve wind speed. The scanning strategy will have a bigger impact on variance measurements (Newman et al., 2016; https://doi.org/10.5194/amt-9-1993-2016) but this is beyond the scope of this paper.

5) *Section 4.2 attempts to describe the influence of shear on the particle microphysics, but insufficient evidence is given to support this. It is obviously difficult to use the Doppler velocity values directly, as these are compromised by the unknown vertical air motion, but the Doppler spectra do show important information. Figure 10 shows one example of the Doppler spectra following one fall streak, and the broadening is consistent with changes in the particle microphysics; the broadening occurs in a temperature range that coincides with the temperature range for the Hallett-Mossop process for secondary ice production (-8 to -3 C). This increase in Doppler spectral width is clearly seen in Figure 3c between 3000 and 2500 m. However, this increase in Doppler spectral width is more or less constant in altitude throughout the entire time period, and not correlated with the wind shear, suggesting that temperature (possibly the Hallett-Mossop process) is responsible for this microphysical process, not shear.*

Thank you for this comment. As shown in Fig. 8 and Fig. 9, the maximum radar reflectivity was observed to coincide with the upper part of the shear layer. This suggests that the shear layer created an ice supersaturated environment, which enabled the falling hydrometeors to grow to larger sizes. As you pointed out correctly, the Doppler spectra (Fig. 10) contains important information regarding the microphysics. The broadening of the Doppler spectrum and the increase in the Doppler velocity (and thus in the particle fallspeed) at 3000 m suggests that riming occurred within this layer as presented in the revised manuscript (page 14, line 264-271): *"Interestingly, the increase in the LDR was collocated with the region of maximum radar reflectivity (2900 m; Fig. 10a), of maximum (negative) Doppler velocity (2900m; Fig. 10a) and the upper part of the shear layer. The spatial coincidence between maximum radar reflectivity, shear layer and increase in LDR was also observed for other fallstreaks (Fig. 3d), suggesting that the shear layer created an ice supersaturated*

environment, within which the hydrometeors grew to larger sizes. The increase in the Doppler velocity might be indicative of riming. Previous studies observed that an increase in the Doppler velocity can be indicative of riming, which leads to a higher terminal fall velocity of particles due to the rapid gain of ice particle mass (e.g., Mosimann, 1995; Kneifel and Moisseev, 2020). This is further supported by the increase in the LDR of the faster falling population of the spectrum as a consequence of the higher particle density."

Indeed, the temperature was in the range of the Hallett-Mossop process, so to account for this we now mention on page 16, line 275-277 that the Hallett-Mossop process was potentially occurring: *"The temperature between 3000 m and 2500 m ranged from -8 °C to -4 °C and was thus in the temperature regime of columnar growth and of the Hallett-Mossop process. Thus, secondary ice particles might be produced upon riming, which could then rapidly grow by vapor deposition into column-like particles."*

6) *Note that Doppler spectra wouldn't necessarily show discrete multiple peaks with secondary ice production in turbulent regions, or if sublimation is occurring (evaporation broadens the size distributions).*

Thank you for pointing this out. We included a sentence describing this effect in the revised manuscript (page 16, line 283-286): *"The analysis of the Doppler spectra showed no evidence of discrete multiple spectral peaks (i.e., the presence of multiple particle populations with different fall speed), which would support the occurrence of secondary ice production. However, turbulent regions or sublimation could broaden the size distributions and thus mask the presence of discrete multiple peaks in the Doppler spectra."*

7) *The conceptual picture shows ice above a supercooled liquid layer, which, although possible, is not that typical for mixed-phase clouds with relatively warm (above -27 C) cloud tops (e.g. Westbrook and Illingworth, 2011; Battaglia and Delanoë, 2013), and is not supported by the remote-sensing observations shown here. The one occasion during P2_unblocked where the base of the supercooled liquid layer is not at the top of the cloud layer seen by the cloud radar is when there is appreciable LWP. LWP of 100 gm-2 implies a liquid layer that is likely to be at least 400 m thick from theoretical adiabatic considerations (e.g. Merk et al., 2016, https://doi.org/10.5194/acp-16-933-2016), which would place the top of the liquid layer at the top of the cloud layer seen by the cloud radar. This means that the observed case study agrees with previous studies.*

Thank you for pointing this out. Indeed, this was a technical mistake in the drawing on our part. We changed the schematic in the revised manuscript, so that the supercooled liquid layer extends up to the cloud top.

8) *The data presented does indicate that low-level blocking influenced the presence of low-level cloud in the valley. The three periods selected showed clearly that low-level cloud was present during blocked low-level flow, but not once this blocking weakened.*

One option would be to investigate the reasons for this further. The radar Doppler velocity plot suggests that the low-level liquid layer is being formed in updrafts, as almost all Doppler velocities appear to be slightly positive (i.e upwards) for this layer. Is this the case? Or is this due to the difficulty in reading the color scale? The typical vertical air velocity in this layer could be determined from either the Doppler spectra (similar to Fig. 10) or from CFADs of Doppler velocity (similar to Fig. 8). If the air motion is upwards, it would still be weak (< 1 m s-1), so would not necessarily counter the blocked flow argument

but be a result of in-valley circulation. Does the LWP correspond to the updraft speed? How about the cloud droplet number or size (Figure 12)?

Thank you for this comment and your suggestions. We extended Section 4.3 in the revised manuscript and investigated the reason for this transition further. Indeed, the updraft velocity seems to play a crucial role for the formation of the feeder cloud (estimated from the maximum Doppler velocity of the spectrum). Higher updrafts were observed during P1_bl and P3_bl, when a low-level feeder cloud was present (page 18, line 310-313): *"Indeed, the cloud radar indicated the presence of higher Doppler velocities and thus higher updraft velocities during P1_bl (0.5 m s^{-1}) and P3_bl (0.7 m s^{-1}) (Fig. 12). When the blocking weakened and the updraft velocity decreased during P2_unbl (0.37 m s^{-1}), the low-level cloud at Wolfgang dissipated likely due to insufficient upward motion to sustain the production of liquid water."* Furthermore, we calculated correlations between the maximum Doppler velocity and the microphysical properties in the revised manuscript (see Fig. 13 and page 18, line 313-322): *"The correlation plots between different dynamical (mean and maximum Doppler velocity) and microphysical properties (LWC, CDNC, mean diameter) in Figure 13 further support the assumption that the updrafts driven by the in-valley circulation induced the formation of the low-level liquid cloud. Moderate positive Spearman's rank correlation coefficients were observed between the maximum Doppler velocity (vmax) and the LWC(0.42) and CDNC (0.46), whereas a weak correlation was found between the maximum Doppler velocity and the mean diameter D (0.17). Similar correlation coefficients were observed between the mean Doppler velocity and the microphysical properties (not shown). The increase in CDNC with increasing updraft velocity (Fig. 13c) suggests that droplet formation was limited by the vertical velocity that generates supersaturation, i.e. velocity-limited conditions were encountered at Wolfgang. This aspect is dealt with in more detail in a paper by Georgakaki et al. (2020), where they investigated the drivers of droplet formation in mixed-phase clouds using observations from the RACLETS campaign."*
The findings suggest that local updrafts were produced by the in-valley circulation during blocked low-level flow, which were the drivers for the formation of the low-level feeder cloud.

9) *The wind direction changes and speed slows (in general) at Wolfgang during P2, which coincides with precipitation and no low-level liquid water (Figure 7). Is this just because there is enough time for the precipitation to fall before evaporating (shallower subsaturated layer)? Is this precipitation solid or liquid? What is the size distribution?*

As mentioned in Section 4.2 (page 14, line 246-249), this is likely a consequence of the lower extent of the subsaturated layer (maximum radar reflectivity moves to lower altitudes, see Fig. 9), which enabled the hydrometeors to reach the surface prior to complete sublimation during P2_unbl. The amount of precipitation recorded by the disdrometer at Wolfgang was generally low (< 0.2 mm/h). The precipitation reaching Wolfgang was solid in accordance with the temperature slightly below 0 °C (see also ice particles detected by MASC and HOLIMO in Fig. 10). A plot of the particle size distribution of hydrometeors measured by the disdrometer at Wolfgang is shown below in Fig. 2. We included the following sentence in the revised manuscript (caption Fig. 11): *"The particles measured by the disdrometer at Wolfgang were primarily in the size range between 0.5 mm and 1.5 mm (not shown)."*

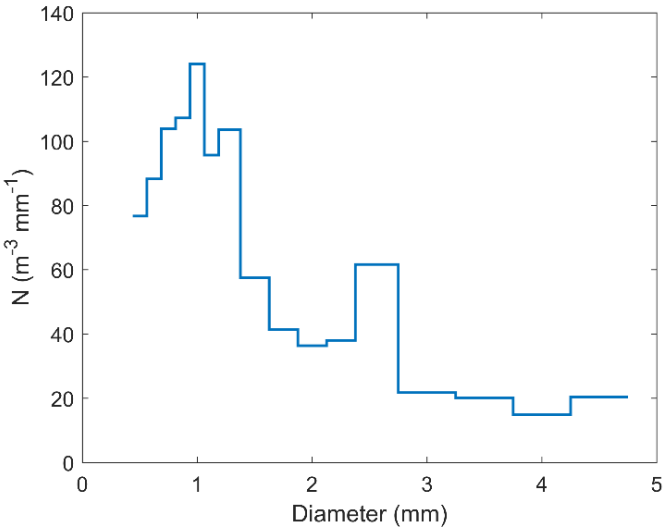

Figure 2: Particle size distribution of hydrometeors measured by the disdrometer at Wolfgang (averaged between 17:45 UTC and 18:40 UTC).

10) *Also of interest is why the seeder-feeder mechanism did not appear to operate in this particular case study, presumably due to the fact that the upper level precipitation rarely fell far enough to benefit. E.g Fig. 12 shows precipitation not quite reaching to 1800 m.*

We assume that the seeder-feeder mechanism only played a minor role for precipitation enhancement in the present case study, as the lower part of the boundary layer was characterized by subsaturated conditions and thus a significant fraction of the hydrometeor mass sublimated before reaching the feeder cloud. However, in the revised manuscript, we included a sentence stating that this effect was important in other cases of the RACLETS campaign (page 20, line 328-332): *"We assume that in the present case study the low-level feeder cloud did not play a crucial role for precipitation enhancement, as a significant fraction of the hydrometeor mass sublimated before reaching the feeder cloud. However, in other cases of the RACLETS campaign, we found that orographically-induced low-level feeder clouds could enhance precipitation through the seeder-feeder mechanism and provide an environment for secondary ice production mechanisms (Ramelli et al., 2020b)."*

11) *Figure 9. Is it likely that the TKE measured close to the surface at Gotschnagrat is representative of the turbulence in the atmosphere? Isn't it more likely to be due to local shear close to surface? What are the wind speeds at this location? The direction is the same as at the surface, but Fig. 5a suggests high wind speeds at this height, is the increase in TKE just due to an increase in wind speed close to the surface? Why would this then correlate with the precipitation rate elsewhere in the valley? How does this relate to the conceptual figure?*

Thank you for pointing this out. It is likely that the high TKE values measured by the 3D sonic anemometer were related to the high wind speed close to the surface and not representative of the turbulence in the atmosphere. Accordingly, we have removed the TKE observations in the revised manuscript.

12) *I'm not convinced of the usefulness of any the correlation coefficients described here. How do they relate to any expected dynamical or microphysical processes? The shear layer appears to coincide with the sublimation zone. For this case study, any attempt to link the surface precipitation to the maximum reflectivity in the profile should at least take the varying sublimation depth into account.*

Thank you for the comment. We agree that it is difficult to relate these coefficients to the dynamical and microphysical processes. We removed Appendix B and the discussions related to the correlation coefficients in Section 4.2 in the revised manuscript. Instead, we focus on the relationships between the vertical velocity and the low-level cloud properties (see also response to review comment #8).

Technical comments

13) *Line 52: Is this wind shear value for wind shear in the horizontal or in the vertical?*

Thank you for this comment. We changed it to "vertical shear in the horizontal wind" in the revised manuscript (page 2, line 53).

14) *Lines 91-92: Do you mean 'the mean ridge height'?*

Thank you for this comment. We changed it to "mean ridge height" (page 4, line 94-95).

15) *Line 116,118: Isn't Vaisala a Finnish company?*

Thank you for pointing this out. We change it in the revised manuscript.

16) *Figure 2 caption: This should state 'taken by the Meteosat 2nd Generation (MSG) satellite'.*

Thank you for pointing this out. We exchanged the satellite picture with a reanalysis plot of the synoptic situation in the revised manuscript.

17) *Line 228: Cloud base? The ice cloud continues to the surface during P1 and P2. Since all ice is falling (precipitating), the ice cloud base is defined in terms of visibility, not in terms of relative humidity (changes in growth or evaporation rate). Hence it is only during P3 that there is an ice cloud base.*

Thank you for pointing this out. We redefined it as onset/beginning of the sublimation layer in the revised manuscript.

Influence of low-level blocking and turbulence on the microphysics of a mixed-phase cloud in an inner-Alpine valley

Fabiola Ramelli[1], Jan Henneberger[1], Robert O. David[2], Annika Lauber[1], Julie T. Pasquier[1], Jörg Wieder[1], Johannes Bühl[3], Patric Seifert[3], Ronny Engelmann[3], Maxime Hervo[4], and Ulrike Lohmann[1]

[1]Institute for Atmospheric and Climate Science, ETH Zurich, Zurich, Switzerland
[2]Department of Geosciences, University of Oslo, Oslo, Norway
[3]Leibniz Institute for Tropospheric Research, Leipzig, Germany
[4]Federal Office of Meteorology and Climatology MeteoSwiss, Payerne, Switzerland

Correspondence: Fabiola Ramelli (fabiola.ramelli@env.ethz.ch) and Jan Henneberger (jan.henneberger@env.ethz.ch)

Abstract. Previous studies that investigated orographic precipitation have primarily focused on isolated mountain barriers. Here we investigate the influence of low-level blocking and shear-induced turbulence on the cloud microphysics and precipitation formation in a complex inner-Alpine valley. The analysis focuses on a mid-level cloud in a post-frontal environment ~~,~~ ~~by combining observations~~ and a low-level feeder cloud induced by an in-valley circulation. Observations were obtained from an extensive set of instruments including ground-based remote sensing instrumentation, in situ instrumentation on a tethered balloon system and ground-based precipitation measurements.

During this event, the boundary layer was characterized by a blocked low-level flow and a turbulent shear layer, which separated the blocked layer near the surface from the stronger cross-barrier flow aloft. Cloud radar observations ~~indicate~~ indicated changes in the microphysical cloud properties within the turbulent shear layer including enhanced linear depolarization ratio (i.e., change in particle shape or density) and increased radar reflectivity (i.e., enhanced ice growth). Based on the ice particle habits observed at the surface, we suggest that ~~needle growth and aggregation~~ riming, aggregation and needle growth occurred within the turbulent layer~~and that collisions~~ . Collisions of fragile ice crystals (e.g., dendrites, needles) and the Hallett-Mossop process might have contributed to secondary ice production.

Additionally, in situ instrumentation on the tethered balloon system observed the presence of a low-level feeder cloud above a small-scale topographic feature, which dissipated when the low-level flow turned from a blocked to an unblocked state. Our observations indicate that the low-level blocking (due to the downstream mountain barrier) ~~caused the low-level flow to ascend the leeward slope of the local topography in the valley, thus producing~~ created an in-valley circulation, which led to the production of local updrafts and the formation of a low-level feeder cloud. Although the feeder cloud did not enhance precipitation in the present case (due to the presence of a subsaturated layer above), we propose that local flow effects such as low-level blocking can induce the formation of feeder clouds in mountain valleys and on the leeward slope of foothills upstream of the main mountain barrier, where they can act to enhance orographic precipitation through the seeder-feeder mechanism.

1 Introduction

Mountains can alter and reorganize incoming weather systems or force air masses to lift and thus produce a large proportion of the Earth's annual precipitation (Roe, 2005). Besides the total amount of precipitation, also its spatial distribution across the mountain range becomes of increasing importance for public warning (e.g., avalanche, flash flood), water resources, hydropower production and winter tourism (Stoelinga et al., 2013). In addition to orographic lifting and the subsequent production of condensate, additional processes are required to efficiently form precipitation-sized particles within the lifetime of the cloud as it crosses the mountain barrier (e.g., Smith, 1979; Frei and Schär, 1998; Roe, 2005; Houze Jr, 2012; Smith, 2019). As such, an extensive knowledge of these physical processes and the interplay between dynamics, microphysics and orography is essential to understand precipitation formation over complex terrain.

Numerous mechanisms have been identified to affect the air flow and enhance orographic precipitation (e.g., Borys et al., 2003; Rotunno and Houze, 2007; Lowenthal et al., 2011; Houze Jr, 2012; Medina and Houze Jr, 2015; Kirshbaum et al., 2018; Smith, 2019). For example, if the air flow impinging on a mountain barrier is sufficiently weak, or the mountain barrier is too high or the atmosphere is stably stratified, the low-level flow might be blocked or diverted around the mountain. As a consequence, a stagnant blocked layer can form in front of the mountain barrier, which extends the effective width of the mountain barrier and causes lifting further upstream (e.g. Rotunno and Ferretti, 2001; Medina and Houze, 2003; Jiang and Smith, 2003). Additionally, a layer of strong shear is usually present at the interface between the blocked layer and the strong cross-barrier flow aloft, which can be the source of turbulent motions. This shear-induced turbulent layer can enhance orographic precipitation (e.g. Houze Jr and Medina, 2005; Medina et al., 2005; Medina et al., 2007) and will be the focus of the present study.

Besides the dynamical response of the air flow to the orography, a wide range of microphysical interactions can occur between cloud droplets, ice crystals and water vapor. For example, individual ice crystals can grow by vapor deposition, can collide and stick together with other ice crystals (aggregation) or can collide with supercooled cloud droplets that freeze upon contact (riming) (e.g. Pruppacher and Klett, 1980; Lohmann et al., 2016). Turbulence and updrafts can accelerate ice growth ~~by~~ through riming and aggregation and thus precipitation fallout, by sustaining the production of supercooled liquid water (Rauber and Tokay, 1991) and by increasing the collision efficiencies between cloud particles (Pinsky et al., 2016). Furthermore, enhanced ice-ice collisions can promote mechanical break-up of ice crystals and lead to the production of a large number of small secondary ice particles (e.g., Vardiman, 1978; Yano et al., 2016). Additionally, riming can also produce secondary ice through the Hallett-Mossop process, which is known to be active at temperatures between -3 °C and -8 °C (Hallett and Mossop, 1974).

In the present study, we investigate the influence of low-level blocking and shear-induced turbulence on the microphysics and precipitation formation of a mixed-phase cloud in an inner-Alpine valley. Previous studies found that flow blocking and shear-induced turbulence can facilitate rapid ice growth and ultimately enhance orographic precipitation (e.g., Marwitz, 1983; Overland and Bond, 1995; Yu and Smull, 2000; Hogan et al., 2002; Neiman et al., 2002; Neiman et al., 2004; Houze Jr and Medina, 2005; Loescher et al., 2006; Olson et al., 2007; Olson and Colle, 2009; Geerts et al., 2011; Medina and Houze Jr, 2015; Grazioli et al., 2015; Aikins et al., 2016). For example, turbulent updraft cells were observed over the Oregon Cascade Mountains in regions where the ~~wind shear~~ vertical shear in the horizontal wind exceeded $10\,\mathrm{m\,s^{-1}\,km^{-1}}$ (Houze Jr and Med-

ina, 2005). Houze Jr and Medina (2005) suggested that these turbulent updraft cells can enhance ice growth through riming and aggregation. Both mechanisms can lead to rapid conversion of condensate to precipitation-sized particles. More recent studies confirmed the findings by Houze Jr and Medina (2005) that turbulent updraft cells enhance ice growth and precipitation (e.g., Medina and Houze Jr, 2015; Geerts et al., 2011; Aikins et al., 2016). However, Geerts et al. (2011) could not draw any conclusions regarding the dominant ice growth processes, due to restrictions in the aircraft flight level. On the other hand, Aikins et al. (2016) proposed depositional growth and aggregation as the dominant ice growth mechanisms for their study rather than riming due to the low amounts of liquid water observed in the shear layer. Thus, the dominant growth process within shear-induced turbulent layers depends on the environmental conditions such as temperature, updraft velocity and the ice crystal ~~size distribution~~and cloud droplet size distributions.

The present work builds on the previous studies that investigated the implications of shear-induced turbulence on the cloud microphysics and precipitation formation and extends the analysis to a more complex terrain. While previous observational studies have mainly focused on the effect of an isolated mountain barrier, we ~~will investigate~~ investigated the role of shear-induced turbulence in an inner-Alpine valley near Davos, Switzerland. The region around Davos, or more generally the Alpine region, is characterized by complex terrain with narrow valleys and multiple mountain barriers, which can cause complex interactions between numerous mechanisms on different scales. This complexity has already been recognized during the Mesoscale Alpine Programme (MAP) (e.g., Rotunno and Houze, 2007). In an environment with a series of parallel mountain ridges, a superposition of upstream and downstream effects can occur. In the present study, we attempt to investigate whether a 'simple' conceptual mechanism as described in Houze Jr and Medina (2005) can also be observed in a complex environment that is embedded between two mountain ridges and which is likely influenced by upstream and downstream effects. In addition, we extend the analysis to lower altitudes, which were inaccessible in previous studies due to limits in the flight levels, by using a tethered balloon system. The balloon-borne profiles can provide information on the microphysical cloud properties in the lowest part of the boundary layer. These questions are addressed in a case study on 7 March 2019, which was observed in a post-frontal air mass during the Role of Aerosols and CLouds Enhanced by Topography on Snow campaign (RACLETS). The multi-instrument analysis is based on (1) wind profiler and wind lidar measurements, (2) observations of a Ka-band polarimetric cloud radar, a Raman lidar and a microwave radiometer, (3) in situ microphysical measurements on a tethered balloon system and (4) ground-based precipitation measurements.

The main measurement locations and instruments are briefly described in Section 2. An overview of the synoptic weather situation and the case study is given in Section 3. Section 4 presents the influence of low-level blocking and shear-induced turbulence on the cloud microphysics and precipitation formation. The findings are discussed in a larger context and presented in a conceptual model in Section 5. A summary of the main findings is given in Section 6.

2 Measurement location and instruments

The RACLETS campaign took place from 8 February 2019 to 28 March 2019 in the region around Davos in the Swiss Alps. The main objective of the campaign was to investigate the pathways of precipitation formation in orographic clouds, cov-

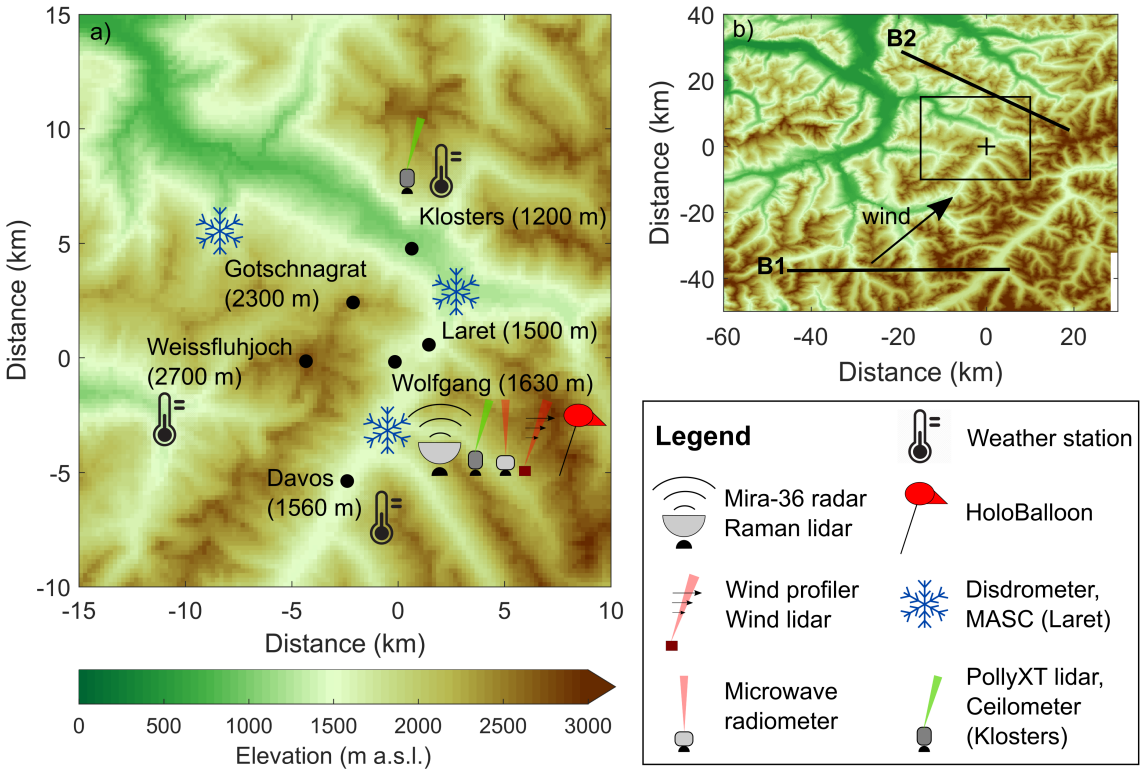

Figure 1. Overview of the measurement location and setup. The geographical location of Davos (black cross) and the surrounding topography is shown in (b). The large-scale wind direction during the event is shown by the black arrow and the relevant mountain barriers are indicated by B1 (upstream mountain barrier) and B2 (downstream mountain barrier). An enlarged section of the measurement sites (black rectangle in b) and the instrument setup are shown in panel (a). The elevation data was obtained from the digital height model DHM25 of the Federal Office of Topography~~swisstopo: https://shop.swisstopo.admin.ch/de/products/height_models/dhm25200, last access: 9 March 2020.~~

ering the entire aerosol-cloud-precipitation-snow distribution process chain, in order to improve our understanding of oro-
90 graphic precipitation. The overall goal of the RACLETS campaign was to use the gained process understanding of orographic clouds to improve regional precipitation forecast in complex terrain. For this purpose, a multi-dimensional set of instruments and measurements was deployed to provide a comprehensive dataset of orographic clouds (see also Ramelli et al., 2020b; Lauber et al., 2020; Mignani et al., 2020; Georgakaki et al., 2020).

2.1 Measurement location

95 A map of the instrument setup and the relevant measurement locations is shown in Figure 1. Davos is located in the Swiss Alps in the eastern part of Switzerland. The Alpine massif is oriented in a southwest-northeast direction and has a mean ridge height of around 3000 m a.s.l. or 2400 m above the surrounding lowlands. The Alps represent a barrier for incoming weather systems, which predominantly approach the measurement location in Davos from northwest or south. During the presented case study,

the ~~weather system came~~ large-scale flow was from south-western direction and thus followed approximately the direction of the Davos valley. Weather systems approaching Davos from the south are influenced by topography to a larger extent, because the main ridge of the Alps is located south of Davos (indicated by B1 in Fig. 1b).

The main measurement locations consist of two mountain-top stations (Weissfluhjoch 2700 m, Gotschnagrat 2300 m), and three valley stations (Wolfgang 1630 m, Laret 1500 m, Klosters 1200 m), which are located within a distance of 10 kilometers (see Fig. 1a). The region around Klosters and Davos is characterized by complex topography. The Klosters valley is oriented from northwest to southeast and the elevation gradually increases from the lowlands (500 m) to 1200 m. In contrast, the Davos valley is oriented in a northeast-southwest direction. The height rapidly increases from Klosters (1200 m) towards Wolfgang (1630 m), before it slowly decreases on the way to Davos (1560 m). In the following, we will briefly describe the relevant instruments, which have been used in the present study.

2.2 Instrument setup

A set of ground-based remote sensing and in situ instruments was installed at Wolfgang to study the microphysical cloud structure (Fig. 1a). A vertically-pointing Ka-band cloud radar Mira-36 (METEK GmbH, Germany, Melchionna et al., 2008; Görsdorf et al., 2015; Löhnert et al., 2015) provided vertical profiles of radar reflectivity factor, Doppler velocity, Doppler spectra, spectral width and linear depolarization ratio (LDR) with a vertical resolution of 31.17 m and a temporal resolution of 10 s. A PollyXT Raman and depolarization lidar (e.g., Engelmann et al., 2016) was deployed to study the aerosol and cloud properties. Moreover, a 14-channel microwave radiometer (HATPRO, Radiometer Physics GmbH, Germany; Rose et al., 2005) provided information about the vertical temperature and humidity profiles as well as the column integrated water vapor content (IWV) and liquid water path (LWP). In situ observations of the low-level microphysical cloud structure were obtained with a tethered balloon system (HoloBalloon; Ramelli et al., 2020a). The main component of the measurement platform is the HOLographic cloud Imager for Microscopic Objects (HOLIMO), which can image cloud particles in the size range of 6 µm to 2 mm (Henneberger et al., 2013; Beck et al., 2017; Ramelli et al., 2020a). It provides information about the phase-resolved number concentration, water content, size distribution and particle shape. Additionally, a ceilometer (CL31, Vaisala, ~~US~~Finland) was installed at Klosters, which was used to identify the height of the cloud base (Fig. 1a).

Observations of the three-dimensional wind fields were obtained with a vertically-pointing radar wind profiler (LAP-3000 Wind profiler, Vaisala, ~~US~~Finland) and a wind lidar (Windcube 100S, Leosphere, France) at Wolfgang (Fig. 1a). The wind profiler had a temporal resolution of 5 min and a vertical resolution of 200 m, whereas the wind lidar provided wind measurements with a higher vertical resolution of 50 m. The wind lidar operated in Doppler Beam Switching (DBS) mode with 4 beams at an elevation angle of 75° and a vertical beam. Additionally, Range Height Indicator scans (RHI) were performed every 30 minutes in four different azimuth directions (0°, 70°, 180° and 250°).

Precipitation was measured using a set of different ground-based precipitation instruments. Three Particle Size Velocity (Parsivel) disdrometers (OTT Parsivel2, OTT HydroMet, Germany; Tokay et al., 2014) were installed at Wolfgang (1630 m), Laret (1500 m) and Gotschnagrat (2300 m), respectively (see Fig. 1a). Parsivel disdrometers can measure the size and the fall velocity of hydrometeors falling through the sample volume independently. The particle size is estimated from the signal attenuation,

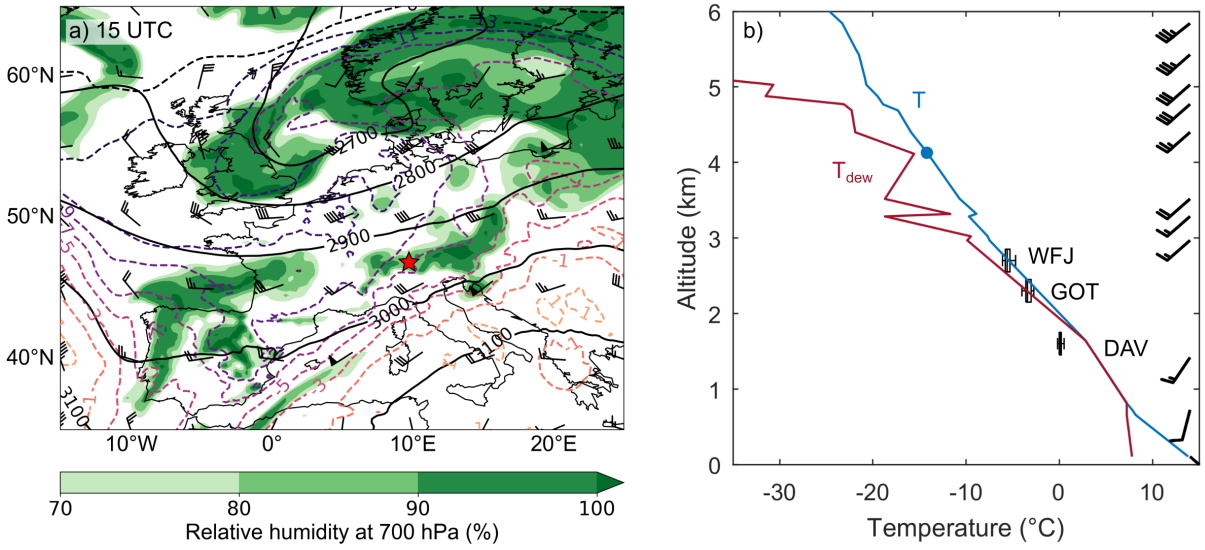

Figure 2. Overview of the synoptic weather situation on 7 March 2019 showing a ~~satellite picture over Europe~~ map of ERA5 reanalysis data at 700-hPa height with a horizontal resolution of 0.25° (a) and the temperature profile of a radiosonde ascent (b). The ~~satellite picture was taken by~~ reanalysis shows the ~~Meteosat~~ relative humidity in percent (colorfill), the temperature in °C (dashed lines), the geopotential height in meters (black lines) and the wind speed and direction in knots (wind barbs) at ~~12~~ the 700 hPa pressure level at 15 UTC (~~Eumetsat~~data obtained from the C3S Climate Data Store; dataset by Hersbach et al., 2018). The 700 hPa pressure level was chosen as it represents the mean Alpine ridge height. The red star indicates the measurement location. The radiosonde was launched from Milan (12 UTC; ~~; last access~~Source: ~~16 March 2020~~UQAM-Montreal Weather Centre) and shows the temperature (blue) and dew point temperature (red) profiles. The boxplots in (b) show the temperature measured at Davos (DAV, 1600 m), Gotschnagrat (GOT, 2300 m) and Weissfluhjoch (WFJ, 2700 m) during the measuement period. The cloud top temperature (-14 °C) and height (4000 m; estimated from cloud radar observations averaged between 17 UTC and 18.30 UTC) are indicated by the blue dot. The wind barbs are shown on the right side.

whereas the particle fall velocity is estimated from the duration of the measured signal. Precipitation particles in the size range between 0.2 mm and 25 mm can be measured by the disdrometer with a temporal resolution of 30 s. Additionally, a Multi-Angle Snowflake Camera (MASC) at Laret took photographs of hydrometeors from three different angles and measured their fall velocity simultaneously (Garrett et al., 2012). The MASC is sensitive to particles in the size range of 100 µm and 10 cm. Lastly, a snow drift station was installed at Gotschnagrat, which provided information about the snow redistribution at the ground and the low-level wind field (Walter et al., 2020).

3 Description of the case study

The ~~weather situation~~ presented case study was measured in a post-frontal environment on 7~~March 2019 was characterized by a~~ March 2019. The synoptic situation over Europe was dominated by an occluding low-pressure system ~~that moved from the~~

~~North Sea towards Scandinaviaand brought~~ (980 hPa) located east of the British Isles. As the low-pressure system continued to propagate towards Scandinavia, it drove a cold front ~~towards Switzerland (Fig. 2a). Ahead of the cold front, a 15~~over the Alps, which passed the measurement location at 8 ~~hPa pressure gradient between the south and north side of the Alps produced a strong foehn event with wind gusts of up to 130 km h^{-1}. The cold front crossed Switzerland from the southwest in the morning and ended the pronounced foehn situation.~~ UTC. Based on observations, rainfall of up to 50 mm was produced on the southern side of the Alps during the passage of the cold front (not shown). ~~Moist~~ By 15 UTC, southwesterly flow in the post-frontal air mass ~~led to light showers~~ continued to advect cold air and moisture into the Alpine region (see Fig. 2a), which produced light precipitation on the south side of the Alps ~~due to orographic lifting. Some spillover precipitation was observed~~ with some spillover precipitation on the lee side (i.e. north side) of the Alps~~and reached the measurement locations in Davos. The presented~~ . The case study was measured in the post-frontal air mass between 16 UTC and 20 UTC, when some spillover precipitation reached the measurement locations in the Davos region.

The temperature at Davos (1600 m) was around 0 °C during the entire observational period, whereas the temperature at Weissfluhjoch (2700 m) decreased from -4.5 °C to -6 °C between 16 UTC and 20 UTC. Due to the lack of a sounding in the Davos area during the measurement period, the vertical temperature profile of a radiosonde ascent from Milan (Italy; at 12 UTC)~~is~~ , which is located 150 km southwest of Davos, is shown instead (Fig. 2b). The sounding in Milan is assumed to be representative of the upper air situation in Davos, as the air flow was from the southwest. In addition, the temperatures measured at Gotschnagrat and Weissfluhjoch were in good agreement with the temperature profile of the radiosonde (within 1 - 2 ~~K~~°C), whereas the temperature observed in Davos was slightly colder. A cloud top temperature of around -14 °C was estimated from the observed temperature profile.

An overview of the microphysical cloud structure is shown in ~~Figures~~ Figure 3 and 4. The cloud radar observations indicate the presence of a mid-level cloud with a cloud top at around 4000 m. The highest reflectivities (> 5 dBZ) were observed between 2500 m and 3500 m (Fig. 3a). The reflectivity decreased below 2500 m, ~~indicating~~ suggesting the presence of a sublimation layer. The Doppler velocity showed mainly regions with negative Doppler velocity (Fig. 3b). Positive Doppler velocities (i.e., updrafts) were only observed after 18 UTC near cloud top and after 19 UTC near the ground. Additionally, several regions of enhanced spectral width were observed (Fig. 3c). High values in the spectral width signal can be the result of enhanced turbulence and/or indicate the presence of multiple particle populations with different fall speeds (e.g., Shupe et al., 2004; Shupe et al., 2006). The linear depolarization ratio (LDR) ranged between -32 dB and -22 dB (Fig. 3d) and provides information about the shape ~~of the~~ and density of cloud particles. A perfectly spherical particle (e.g., small cloud droplet) has no depolarization and thus an LDR of -∞ dB, whereas a particle with a high aspect ratio has a LDR close to 0 dB. ~~Furthermore, the~~ The LDR of a specific hydrometeor type depends on the elevation angle (North et al., 2014). Since a vertically-pointing cloud radar was used in this study, the observed LDR signal can only differentiate between isometric particles (e.g., droplets, plates, dendrites) and prolate particles (e.g., needles, columns). Furthermore, the LDR depends on the particle refractive index. Liquid water has a higher refractive index (0.93) than ice (0.197) (Houze Jr, 2014). For ice particles, the refractive index is related to the particle density, such that hail and graupel have a higher refractive index compared to snowflakes (Bringi and Chandrasekar, 2001). Therefore, changes in the LDR are indicative for changes in the particle shape and/or particle density (e.g. riming). The LDR

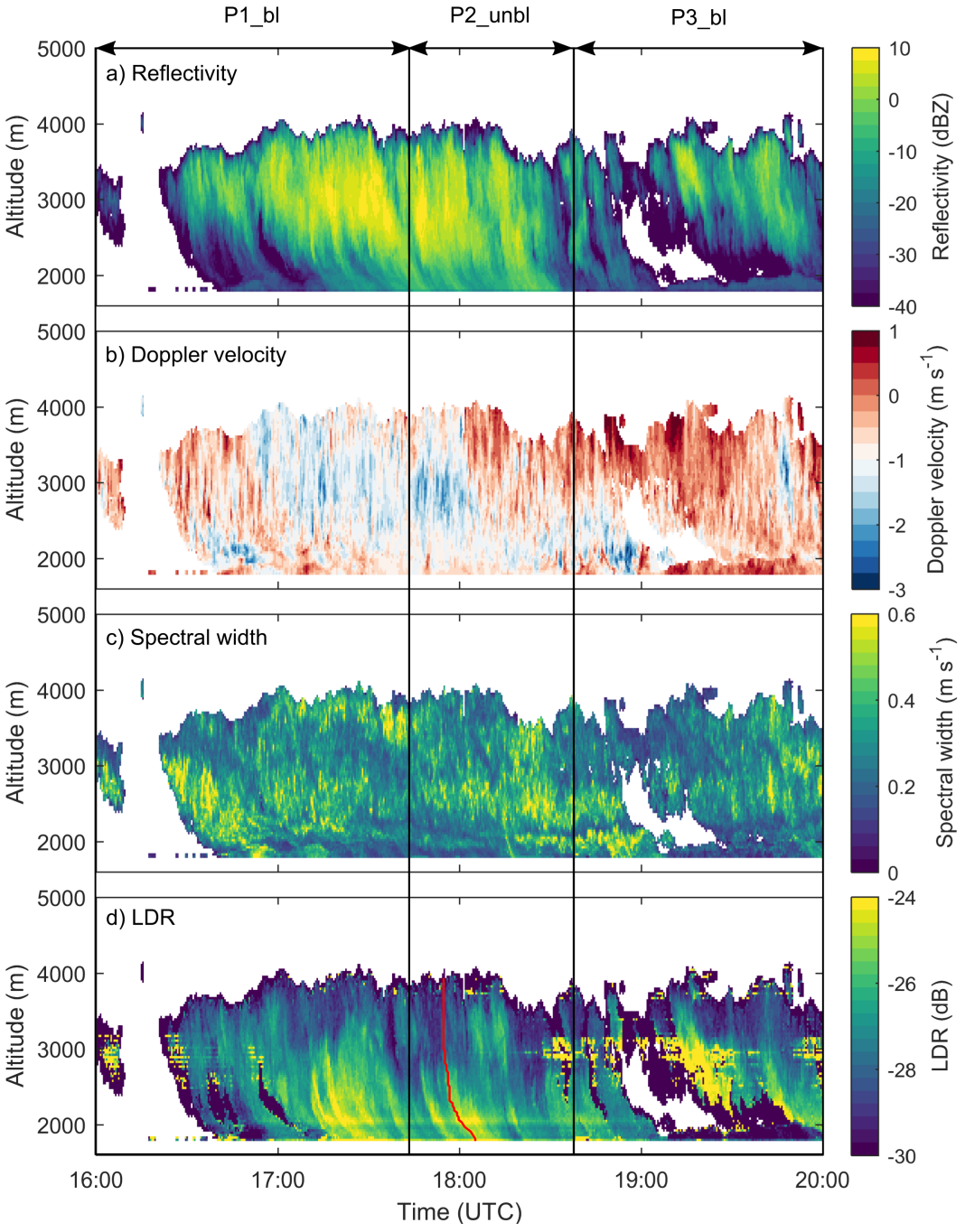

Figure 3. Cloud radar observations of the radar reflectivity (a), Doppler velocity (b), spectral width (c) and linear depolarization ratio (d) measured on 7 March 2019. Note that the colorbar in (b) is centered at -1 m s^{-1} to approximately account for the hydrometeor fall speed. The red line in panel (d) indicates the track of the 18 UTC LDR-fallstreak, which was investigated in Fig. 10. The measurement period is divided into three periods, where P1_bl and P3_bl indicate blocked low-level flow and P2_unbl indicates unblocked low-level flow (see Sect. 4.1 for more details).

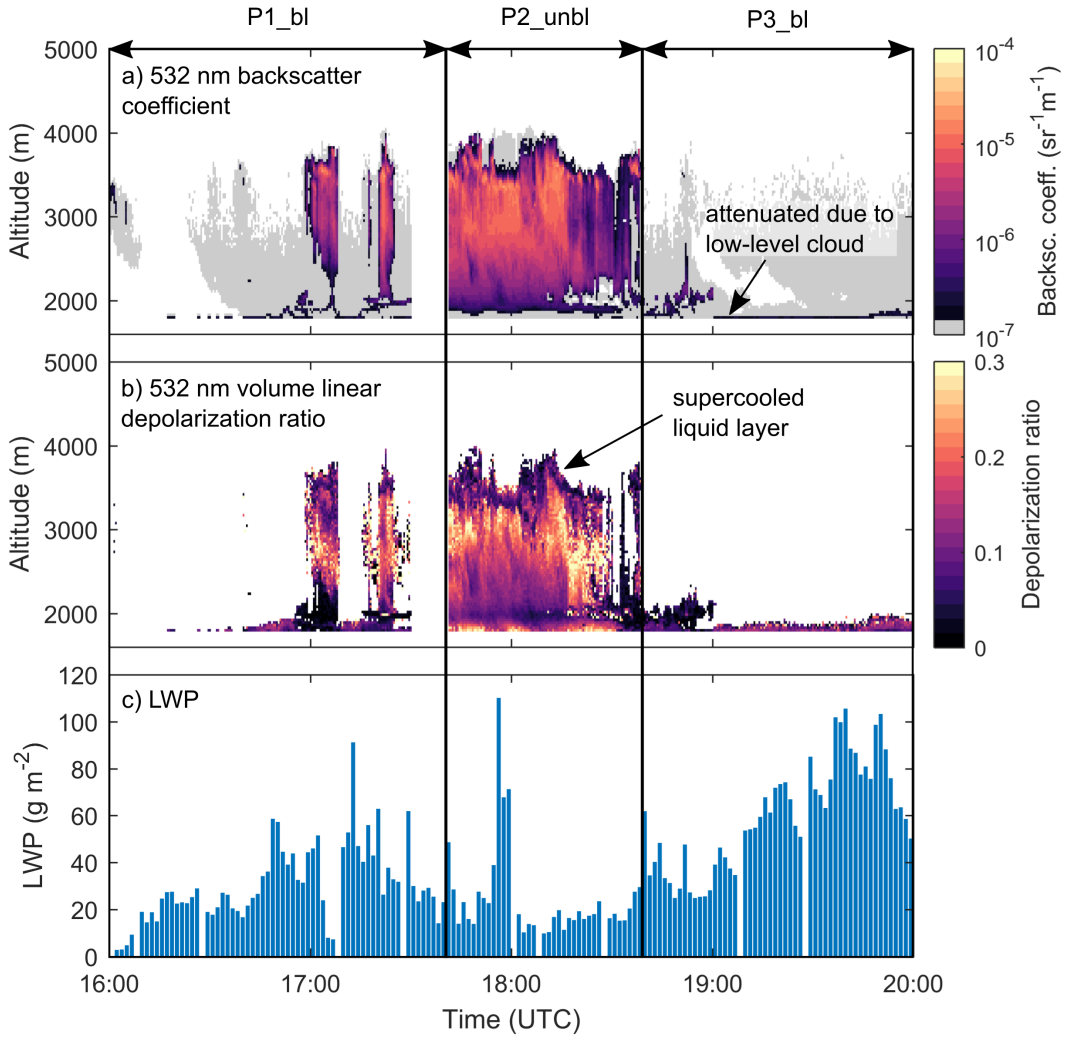

Figure 4. Observations of the lidar attenuated backscatter coefficient (a), the lidar linear depolarization ratio (b) and the liquid water path measured by the microwave radiometer (c). The measurement period is divided into three periods, where P1_bl and P3_bl indicate blocked low-level flow and P2_unbl indicates unblocked low-level flow (see Sect. 4.1 for more details).

signal was enhanced locally in some fallstreaks at altitudes below 3000 m ~~, which is indicative of a change in the particle shape.~~ (Fig. 3d). The band of enhanced LDR at 2100 m, which was visible during the entire measurement period, shows the effects of ground clutter (i.e., echos received from objects on the ground or sidelobes reflected from nearby mountains).

The lidar signal was mainly attenuated due to the presence of a low-level liquid cloud (Fig. 4). When the low-level liquid cloud dissipated (17:45 - 18:40 UTC), the lidar signal indicated the presence of an embedded liquid layer at an altitude of around 3500 m. This can be seen by the enhanced attenuated backscatter signal (Fig. 4a) and the low lidar depolarization ratio (Fig. 4b). ~~The measured LWP was generally below~~ Liquid water might also be present below 3500 m, but in lower concentrations.

Indeed, the LWP measured by the microwave radiometer ranged between 20 g m^{-2} and 100 g m^{-2} during the measurement period (Fig. 4c), suggesting that liquid water was present in the mid-level cloud.

The case study was divided into three periods: Period P1_bl (16:00 UTC - 17:45 UTC) and ~~period~~ P3_bl (18:40 UTC - 20:00 UTC) were characterized by blocked low-level flow and the presence of a low-level liquid cloud at around 2000 m~~, whereas the~~ . The low-level blocking weakened and the low-level feeder cloud dissipated during period P2_unbl (17:45 UTC - 18:40 UTC). In the following, we characterize the dynamics of the flow during the measurement period (Section 4.1). In a second step, we investigate the influence of shear-induced turbulence on the cloud microphysics and precipitation formation (Section 4.2). Lastly, the role of the low-level blocking for the formation of a low-level feeder cloud is discussed in Section 4.3.

4 Results

4.1 Low-level flow blocking ~~triggering~~ and wind shear ~~and turbulence~~

~~Vertical profiles of wind speed and direction (a, b) and wind shear (c, d) measured by the radar wind profiler (left) and wind lidar (right). The vertical wind shear was calculated from the wind observations, considering changes in the scalar wind speed between two adjacent height levels.~~The horizontal wind fields were measured with a radar wind profiler and a wind lidar at Wolfgang (Fig. 5). Both wind profiler and wind lidar data are shown, as the wind lidar was attenuated during most of P1_bl and P3_bl due to the presence of a low-level liquid cloud (see Section 4.3). The wind speed measured by the wind profiler increased from around 4 m s^{-1} at 2200 m up to 18 m s^{-1} at 3500 m (Fig. 5a). The wind lidar revealed a second layer of increased wind speed between 2500 m and 3000 m (Fig. 5b), which was not captured by the wind profiler due to its lower resolution. The layer of increased wind speed lowered between 17:00 UTC and 18:30 UTC, suggesting stronger downward propagation of the cross-barrier flow. The large-scale wind direction was from the southwest. Only in the lowest 100 m of the boundary layer, a flow from the northeast was observed by the wind lidar.

The counterflow at low levels with respect to the large-scale flow as well as the low wind speed close to the surface are indicative of blocked low-level flow (e.g., Houze Jr and Medina, 2005). More specifically, the low-level flow at Wolfgang might have been too weak to ascend over the mountain barrier located downstream of Wolfgang (B2 in Fig. 1b) and might have generated a counterflow when it impinges on the mountain barrier. To test this hypothesis and to study the observed pattern in the low-level wind field in more detail, wind measurements from different valley and mountain-top weather stations around Davos and Klosters were analyzed (Fig. 6). Several valley stations (Davos, Davos Seehornwald, Wolfgang, Klosters Gatschiefer) observed the presence of a counterflow (i.e., wind from northeastern direction), indicative of blocked low-level flow. The wind pattern at Klosters Madrisa, which is located immediately below the mountain barrier B2, was more diverse, showing large variations in the prevailing wind direction. The mountain-top stations (Weissfluhjoch, Gotschnagrat, Klosters Sant Jaggem) observed wind from the south and southwestern direction in accordance with the large-scale wind direction. Therefore, the observed wind pattern at the different locations support the hypothesis of a blocked low-level flow. It is important to note that a counterflow was only observed during P1_bl and P3_bl at the valley stations in Davos (Davos, Davos Seehornwald, Wolfgang), indicating that the low-level flow changed from a blocked (P1_bl, P3_bl) to an unblocked (P2_unbl) state during the event (see also Fig. 7

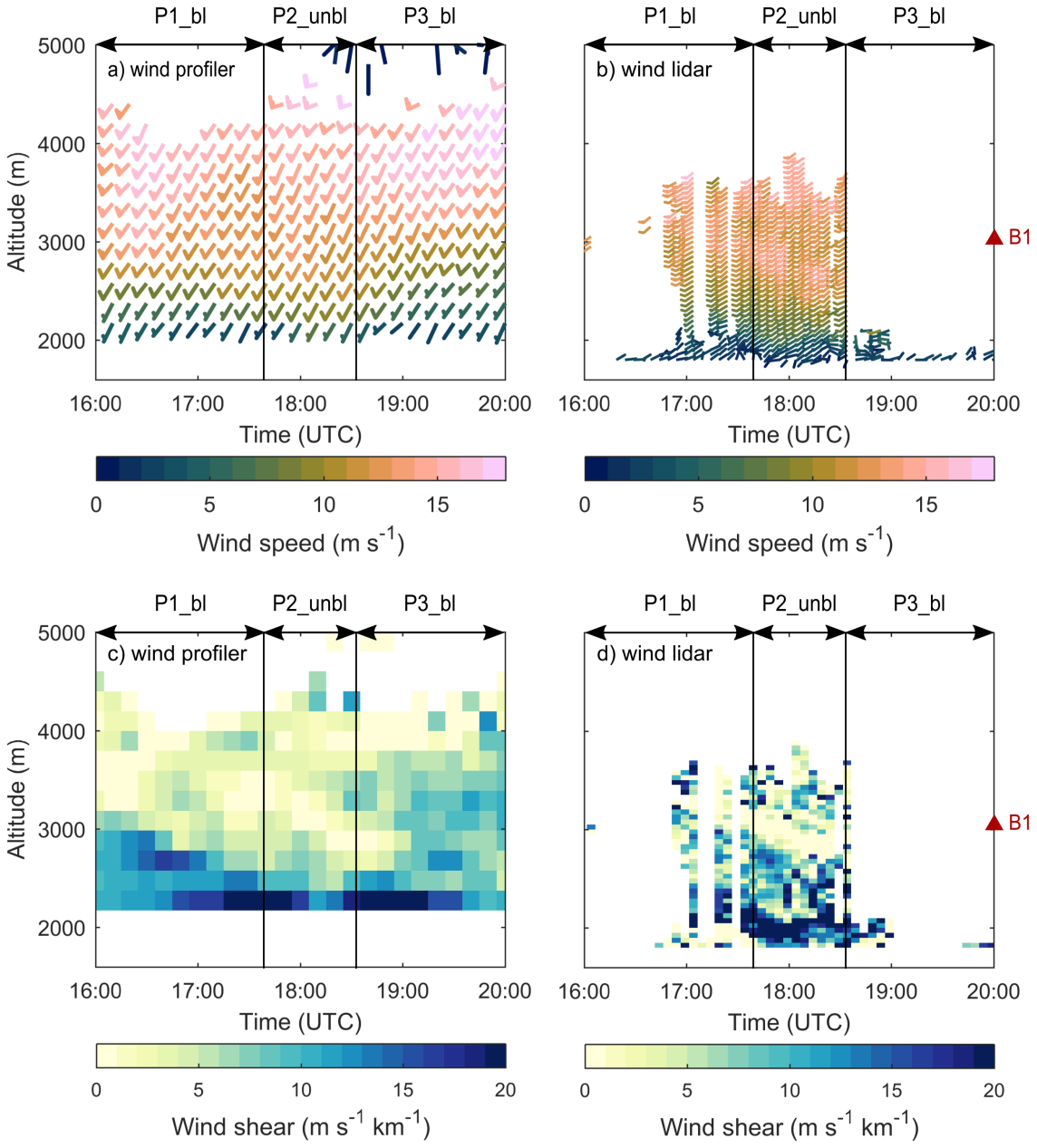

Figure 5. Vertical profiles of wind speed and direction (a, b) and vertical shear in the horizontal wind (c, d) measured by the radar wind profiler (left) and wind lidar (right). The vertical wind shear was calculated from the wind observations, considering changes in the horizontal wind speed between two adjacent height levels. The red triangle symbol on the right side indicates the mean height of the upstream mountain barrier B1 (see Fig. 1b).

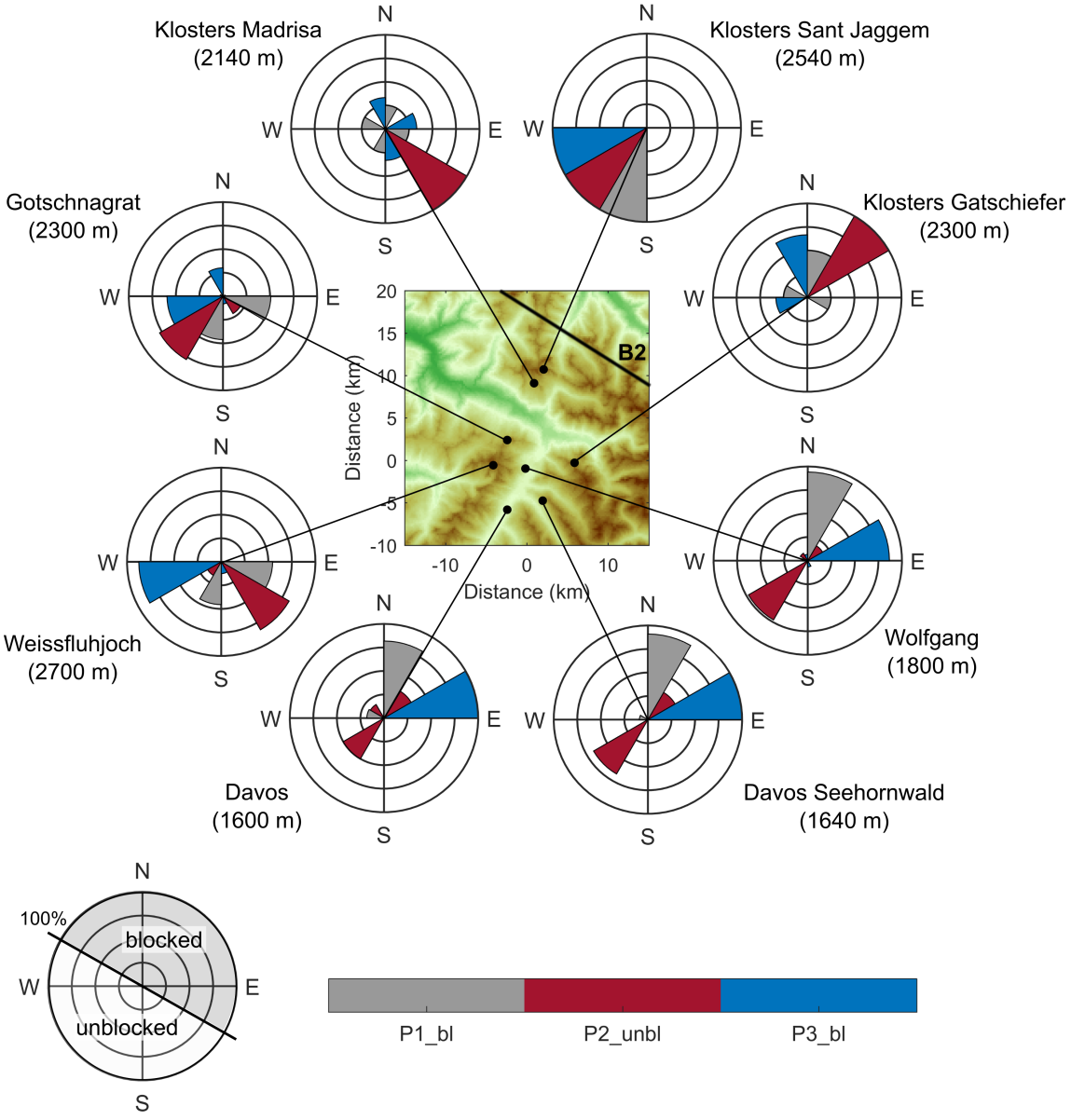

Figure 6. Wind observations at different weather stations around Davos and Klosters, indicating the wind direction observed during the time periods P1_bl (gray), P2_unbl (red) and P3_bl (blue). The wind directions in the different periods were normalized and binned in sectors of 90° (NE, SE, SW, NW). Each line indicates 25%. The example wind rose on the bottom left ~~indicates~~ shows the wind directions during a blocked (gray) / unblocked (white) low-level flow in the Davos valley. The wind observations at the weather stations in Davos had a temporal resolution of 10 min, whereas the stations around Klosters had a temporal resolution of 30 min. The measurements at Wolfgang were obtained from the wind lidar observations at an altitude of 1800 m and the measurements at Gotschnagrat from a 3D ultrasonic anemometer that was an integral part of the snow drift station.

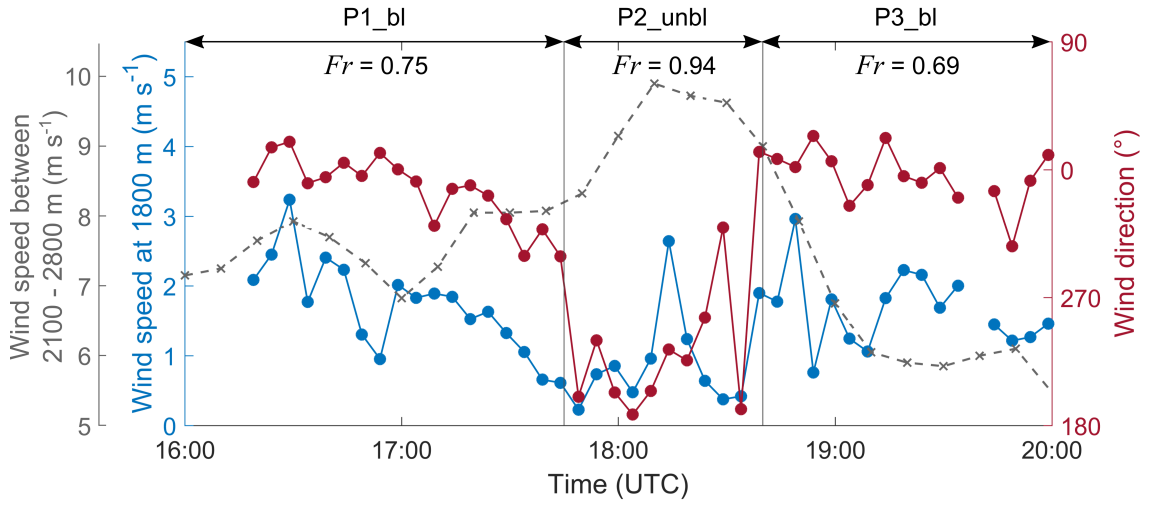

Figure 7. Temporal evolution of the wind speed (blue) and wind direction ~~in azimuth degrees~~ (red) at Wolfgang obtained from the wind lidar measurements at an altitude of 1800 m. The mean wind speed between 2100 m and 2800 m (gray) measured by the wind profiler at Wolfgang is shown as a proxy for the strength of the downward propagating cross-barrier flow. The Froude numbers (Fr) for the different periods are indicated at the top (see Appendix A for calculations).

for the temporal evolution at Wolfgang). The flow at Klosters Gatschiefer was still blocked during P2_unbl, suggesting that the blocking became weaker and moved closer to the mountain barrier B2 located downstream.

From a theoretical perspective, the Froude number can be used to estimate whether a flow that encounters a mountain barrier can pass over the mountain barrier or not (Smith, 1979; Durran, 1990; Rotunno and Houze, 2007; Houze Jr, 2012). The Froude number Fr is given by the following equation:

$$Fr = \frac{U}{hN} \tag{1}$$

where U is the wind speed perpendicular to the mountain barrier, h is the height of the mountain barrier and N is the Brunt-Väisälä frequency (Colle et al., 2013). The Froude number was below 1 for all periods (see Appendix A and Fig. 7), indicating that the low-level flow was blocked. The Froude number increased from 0.75 during P1_bl to 0.94 during P2_unbl (Fig. 7), suggesting that the blocking became weaker during P2_unbl. We will refer to period P2_unbl as unblocked flow, as no counterflow was observed during this period at Wolfgang (Fig. 7), even though it can be seen that the flow at low levels was still slowed down and the Froude number was slightly below 1. ~~Thus, period~~ Period P2_unbl could also be regarded as a weaker blocking.

The wind profiler and wind lidar indicated the presence of a layer of strong vertical wind shear ($>10\,\mathrm{m\,s^{-1}\,km^{-1}}$), which separated the blocked layer from the stronger cross-barrier flow (Fig. 5c, d). The shear layer descended from 3000 m to 2000 m between 16 UTC and 18 UTC (Fig. 5c) in accordance with the weaker blocking and stronger downward propagation of the cross-barrier flow ~~. As the~~ (Fig. 7). As the influence of the downward propagating cross-barrier flow weakened and the

strength of the low-level blocking increased again at around 18:30 UTC, the shear layer ascended (Fig. 5c). Thus, the height of the shear layer ~~is~~ might be determined by a delicate balance of upstream (e.g., blocking) and downstream (e.g., cross-barrier flow) effects, as Wolfgang is located in an inner-Alpine valley and surrounded by multiple mountain barriers. Sloping shear features have also been observed in connection with synoptic scale frontal systems (e.g. Keyser and Shapiro, 1986; Chapman and Browning, 2001), where similar vertical wind shear values have been measured (Chapman and Browning, 2001) . The presented observations cannot provide conclusive evidence about whether the observed wind and shear patterns were orographically or synoptically driven. We suggest that the sloping shear feature was influenced - at least to some extent - by the orography, as the height of the shear layer was related to the altitude of the upstream mountain barrier B1 and the strength of the blocking and downward propagating cross-barrier flow (Fig. 5c, d and Fig. 7).

Regardless of the formation mechanism, wind shear can be a source of turbulence and ~~can~~ have important implications for cloud microphysics. Houze Jr and Medina (2005) defined a critical threshold of $10\,\mathrm{m\,s^{-1}\,km^{-1}}$ for the formation of shear-induced turbulent cells. The observed wind shear ($10 - 20\,\mathrm{m\,s^{-1}\,km^{-1}}$) was above this threshold value in the entire shear layer, suggesting that turbulent cells were embedded within the shear layer. In the following section, we will characterize the microphysical cloud structure and investigate the influence of shear-induced turbulence on the cloud microphysics and precipitation formation.

4.2 Influence of shear-induced turbulence on the cloud microphysics

Contour frequency by altitude diagrams (CFADs) are a useful tool for analyzing the magnitude and the vertical frequency distribution of cloud properties (e.g., Yuter and Houze Jr, 1995). CFADs of the cloud radar reflectivity (a, b), spectral width (c, d) and LDR (e, f) are shown in Figure 8 averaged over sub-periods of P1_bl (left) and P2_unbl (right). A strong increase in the radar reflectivity was observed near cloud top (Fig. 8a, b), indicative for ice formation and growth between 4000 m and 3500 m. Since the region of rapid increase in radar reflectivity was coincident with the height of the supercooled liquid layer measured by the Raman lidar (~~L~~ L in Fig. 8a, b), it is likely that this supercooled liquid layer played an important role for ice nucleation and initial ice growth. The cloud particles continued growing below 3500 m until they reached a sublimation layer, which was identified by the layer of decreasing radar reflectivity~~and also used as definition for cloud base. The cloud base~~ . The sublimation layer lowered between P1_bl and P2_unbl (Fig. 9), likely as a consequence of the stronger downward propagating cross-barrier flow and the subsequent lowering of the shear layer. Consequently, the extent of the sublimation layer decreased between P1_bl (800 m) and P2_unbl (400 m) (Fig. 8a, b), which enabled the hydrometeors to reach the surface prior to complete sublimation (Fig. 9). The highest radar reflectivities were observed within the upper part of the turbulent shear layer (marked with S_1 and S_2 in Fig. 8), suggesting that turbulence created updrafts high enough for exceeding ice saturation and thereby enhanced ice growth. ~~The turbulent kinetic energy (TKE) measured by a 3D ultrasonic anemometer at Gotschnagrat (2300 m) increased from $0.1\,\mathrm{m^2\,s^{-2}}$ to $0.4\,\mathrm{m^2\,s^{-2}}$ between P1_bl and P2_unbl as the shear layer lowered (Fig. 9). The~~ The CFADs of the spectral width (Fig. 8c, d) show two local maxima embedded within the shear layer (at 2500 m and at 2000 m), ~~indicating the presence of a broad hydrometeor size distribution within those regions,~~ which can arise from enhanced turbulence and/or the presence of multiple particle populations with different fall velocities. Additionally, an increase in the LDR was observed

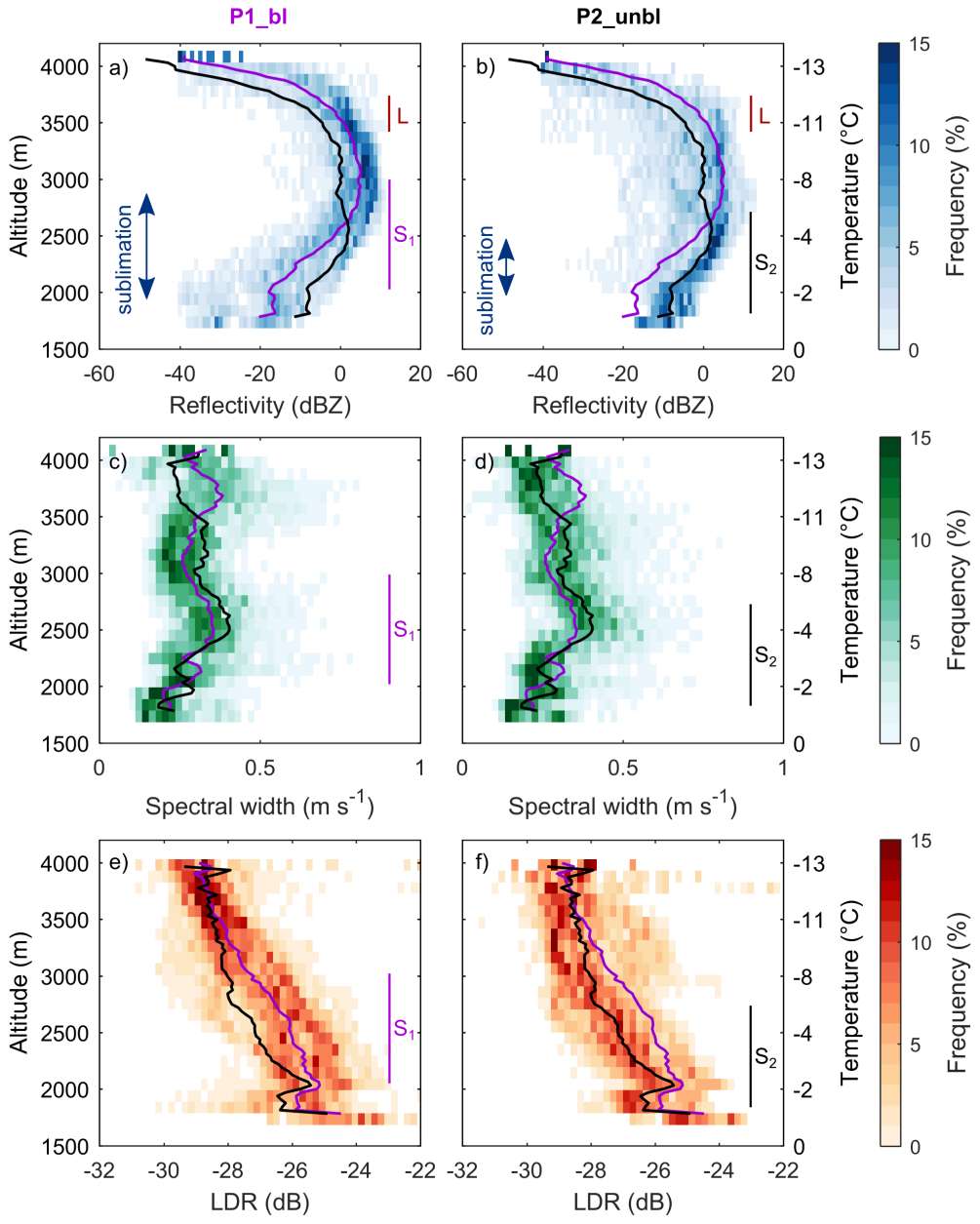

Figure 8. CFADs of the radar reflectivity (a, b), spectral width (c, d) and linear depolarization ratio (e, f) averaged over sub-periods of P1_bl (left, 17 UTC - 17:45 UTC) and P2_unbl (right, 17:45 UTC - 18:30 UTC). The following bin sizes were applied: (1) radar reflectivity from -40 dBZ to 20 dBZ in 1 dBZ intervals, (2) spectral width from 0 m s^{-1} to 0.8 m s^{-1} in 0.02 m s^{-1} intervals and (3) LDR from -32 dB to -22 dB in 0.2 dB intervals. A height interval of 100 m was used for all radar properties. The solid lines represent the mean vertical profile of P1_bl (purple) and P2_unbl (black). The temperature profile measured by the radiosonde is shown on the right y-axis. The extent of the shear layer (S_1, S_2, from wind profiler), the supercooled liquid layer (~~L~~L, from cloud lidar) and the sublimation layer (blue arrow, from cloud radar) are indicated.

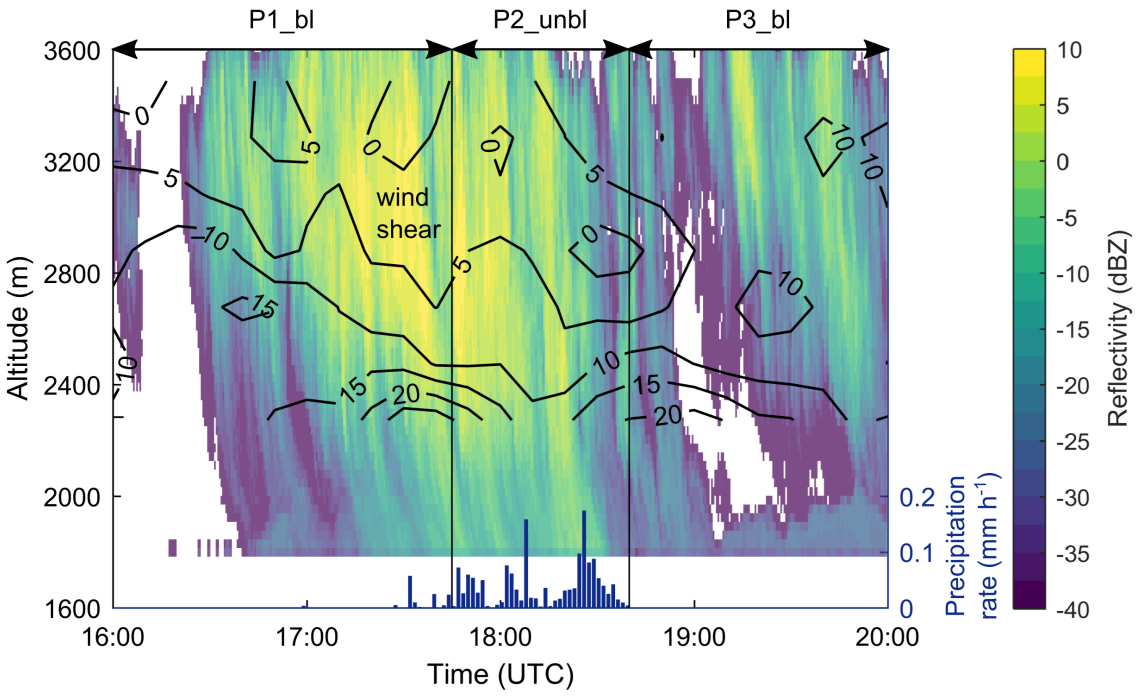

Figure 9. Temporal and spatial evolution of the vertical wind shear (in m s^{-1} km^{-1}, black contour lines), the radar reflectivity (colorfill) and the precipitation rate (blue bars). The wind shear was calculated from the wind profiler observations (Fig. 5) and the precipitation rate was measured with a disdrometer at Wolfgang (1630 m).

within the shear layer (Fig. 8e, f), which is indicative of a change in the hydrometeor shape ~~. Temporal and spatial evolution of the vertical wind shear (in m s^{-1} km^{-1}, black contour lines), the radar reflectivity (colorfill), the TKE (red line) and the precipitation rate (blue bars). The wind shear was calculated from the wind profiler observations (Fig. 5). The precipitation rate was measured with a disdrometer at Wolfgang (1630 m) and the TKE was measured with a 3D ultrasonic anemometer at Gotschnagrat (2300 m). Correlation coefficients between the different parameters (shear layer, radar reflectivity, precipitation) were calculated in Appendix ?? and indicated moderate to strong correlations significant at the 5 % level.Thus, (1) the spatial coincidence of the shear layer and the maximum reflectivity (Fig. 9), (2) the temporal coincidence of the precipitation and the lowering of the shear layer and cloud base (Fig. 9) and (3) the moderate to strong correlations between dynamics, microphysics and precipitation parameters (Appendix ??) suggest that the processes active within the turbulent shear layer enhanced ice growth and precipitation formation.~~or density.

To further explore the microphysics within the turbulent shear layer, the Doppler spectra of the radar reflectivity and LDR along the 18 UTC fallstreak (Fig. 10; highlighted by red line in Fig. 3d) and the surface-based hydrometeor particles observations (Fig. 11) were analyzed. ~~As mentioned in Section 3, the LDR can provide information about the shape of cloud particles. A~~ A mean LDR of around -28 dB was observed near cloud top (Fig. 10b), which is characteristic for oblate particles such as

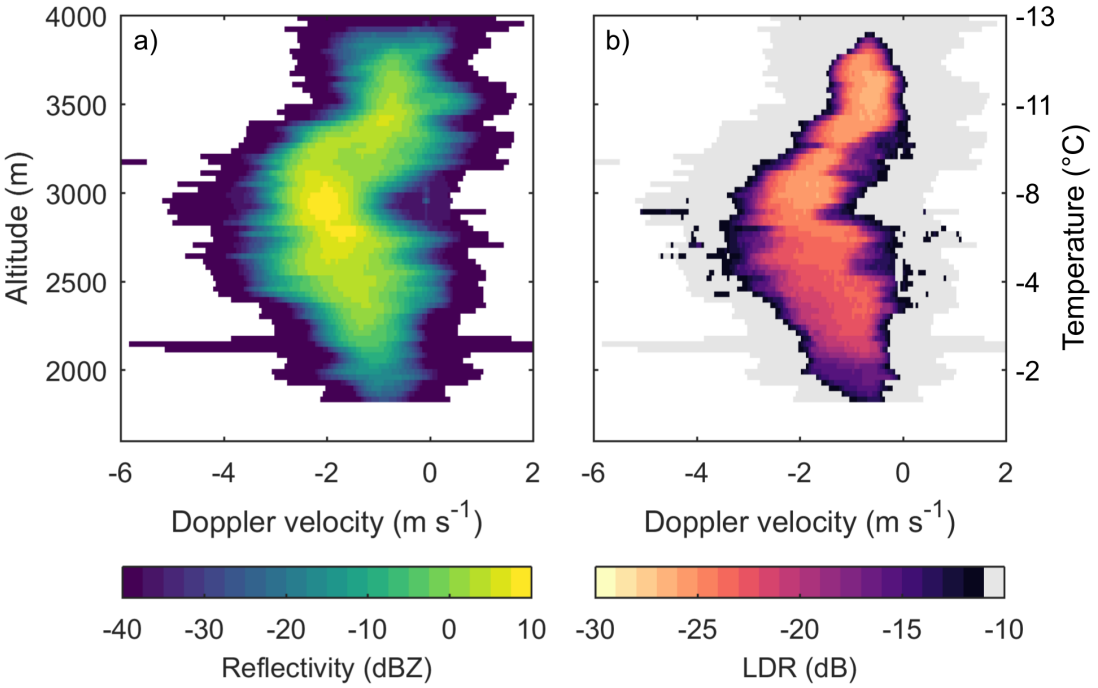

Figure 10. Vertical profile of the radar reflectivity (a) and LDR (b) Doppler spectra along the LDR-fallstreak at 18 UTC averaged over 1 min (see red line in Fig. 3d). LDR values larger than -10 dB are shown in gray. The temperature profile measured by the radiosonde is shown on the right y-axis.

dendrites and plates (e.g., Myagkov et al., 2016; Bühl et al., 2016). This is in agreement with the ice habit expected to form at a cloud top temperature of -14 °C (Magono and Lee, 1966; Bailey and Hallett, 2009) and with the ice particles observed by the MASC at the surface (see D in Fig. 11a). Since a rather constant LDR was observed between 4000 m and 3000 m (Fig. 10b), we assume that the ice crystals grew in size by vapor deposition without changing their habit. Below 3000 m, the LDR of the faster falling part of the spectrum increased up to ~~-20~~ -21 dB ~~within the fallstreak~~ (Fig. 10b) ~~.~~ and the spectrum broadened (Fig. 10a). Interestingly, the increase in the LDR was collocated with the region of maximum radar reflectivity (2900 m; Fig. 10a)~~.~~ , of maximum (negative) Doppler velocity (2900 m; Fig. 10a) and the upper part of the shear layer. The spatial coincidence between maximum radar reflectivity, shear layer and increase in LDR was also observed for other fallstreaks (Fig. 3d), suggesting that the ~~turbulent shear layer did not only enhance ice growth but also contributed to a change in the cloud particle shape. An~~ shear layer created an ice supersaturated environment, within which the hydrometeors grew to larger sizes. The increase in the Doppler velocity might be indicative of riming. Previous studies observed that an increase in the ~~LDR can be explained by the presence of needles, columns and/or irregular ice particles . Here we propose different mechanisms, which could have contributed to an~~ Doppler velocity can be indicative of riming, which leads to a higher terminal fall velocity of particles due to the rapid gain of ice particle mass (e.g., Mosimann, 1995; Kneifel and Moisseev, 2020). This is further supported by the

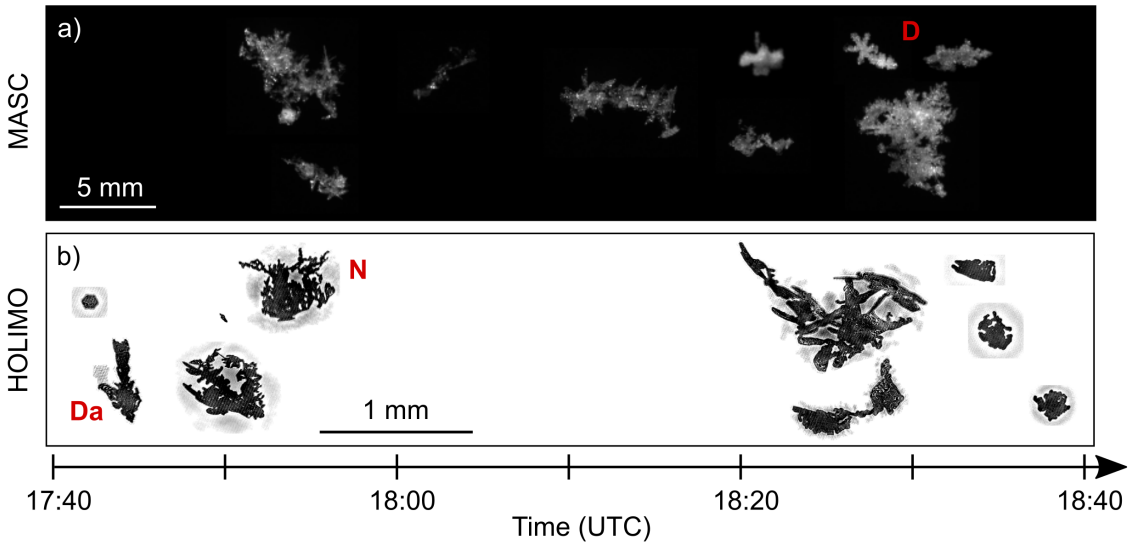

Figure 11. Photographs of ice crystals and snow particles, which have been taken with the MASC (a) and HOLIMO (b). No observations of HOLIMO were available between 17:50 UTC and 18:20 UTC. Please note the different size scale of the particles observed by the MASC and HOLIMO. Examples of crystal types observed by the MASC and HOLIMO are highlighted in red: dendrites (D), dendritic arm (Da), ice particles with needle-like structures (N). The hydrometeors measured by the disdrometer at Wolfgang were primarily in the size range between 0.5 mm and 1.5 mm (not shown).

increase in the ~~observed LDR signal. Firstly, the~~ LDR of the faster falling population of the spectrum as a consequence of the higher particle density. In addition, turbulence within the shear layer could increase the number of collisions between ice particles and promote the formation of aggregated particles (e.g., Pinsky and Khain, 1998). Indeed, the hydrometeors observed by the MASC and HOLIMO show indications of rimed particles and large aggregates (Fig. 11), suggesting that both processes were occurring.

The temperature between 3000 m and 2500 m ranged from -8 °C to -4 °C and was thus in the temperature regime of ~~column/needle growth~~ columnar growth and of the Hallett-Mossop process. Thus, ~~needles might have grown on the existing ice particles while they fell through that cloud layer. Indeed~~secondary ice particles might be produced upon riming, which could then rapidly grow by vapor deposition into column-like particles. These particles would be characterized by higher LDR values. Furthermore, the ice particles observed by the HoloBalloon platform ~~near the ground~~ show indications of needle-like structures (e.g. ~~, at 17:50 UTC;~~ N in Fig. 11b), which might have grown on the existing ice particles while they fell through that cloud layer. If fragile ice crystals such as dendrites or needle-like structures collide with large ice particles within the turbulent shear layer, small ice fragments might break off and lead to the production of secondary ice particles upon collision (e.g., Vardiman, 1978; Yano et al., 2016). For example, the ice ~~particles~~ particle measured by HOLIMO at 17:45 UTC could be a dendritic arm that broke off upon collision ~~. Small secondary ice particles could then rapidly grow by vapor deposition in the water-saturated environment into column-like particles, which are characterized by a higher LDR. However, the~~ (see Da in Fig. 11). The

analysis of the Doppler spectra showed no evidence of discrete multiple spectral peaks (i.e., the presence of multiple particle populations with different fall speed), which would support the occurrence of secondary ice production. ~~Lastly, turbulence can also increase the generation of large ice particles (e.g., Pinsky and Khain, 1998), for example, when multiple ice crystals collide and stick together (aggregation). Aggregation is most efficient at temperatures higher than -10 °C, because of the higher sticking efficiency due to the presence of a thicker quasi-liquid layer at warmer temperatures (e.g., Lohmann et al., 2016). Thus, if the aggregated particles that formed in the turbulent shear layer were irregular, this could explain the increased LDR.Indeed, the MASC indicated the presence of large irregular aggregates between 17:40 UTC and 18:40 UTC (Fig. 11a).~~ However, turbulent regions or sublimation could broaden the size distributions and thus mask the presence of discrete multiple peaks in the Doppler spectra.

For a more sophisticated analysis, a larger number of particles would be necessary, but due to the moderate precipitation rate at Wolfgang and Laret, only a limited amount of ice and snow particles ~~was~~ were observed. However, in general, the in situ and surface observations of ice particles support the radar-based assumptions above, in that (1) dendrites formed near the cloud top and (2) riming, aggregation and needle growth occurred within the turbulent shear layer. It remains unclear whether the Hallett-Mossop process and mechanical break-up in ice-ice collisions contributed to the formation of secondary ice particles ~~.~~ ~~Photographs of ice crystals and snow particles, which have been taken with the MASC (a) and HOLIMO (b). No observations of HOLIMO were available between 17:50 UTC and 18:20 UTC. Please note the different size scale of the particles observed by the MASC and HOLIMO.~~(see also Sect. 5).

4.3 Flow blocking as a driver for the formation of low-level feeder clouds

In the last part of this study, we focus on the lower part of the boundary layer and investigate the role of low-level blocking for the formation of a low-level feeder cloud. The low-level cloud structure was observed with the measurement platform HoloBalloon. Vertical profiles of the in situ cloud properties are shown in Figure 12. The ~~cloud droplet number concentration (CDNC~~liquid water content (LWC) showed a rather inhomogeneous cloud structure during P1_bl. Cloud swaths with a ~~CDNC~~ cloud droplet number concentration (CDNC) of up to 100 cm^{-3} alternated with "cloud-free" regions with low CDNC~~(Fig. 12a). The mean cloud droplet diameter ranged between 10 m and 17 m (Fig. 12b) and was generally larger when the CDNC was low.~~ . No vertical profiles were performed between 17:50 UTC and 18:20 UTC, because the low-level cloud dissipated during this time period. This is also visible from the cloud lidar signal, which was not attenuated during P2_unbl in the lower part of the boundary layer (see Fig. ~~12 and Fig. 4a~~4a, b). A second low-level cloud formed during P3_bl. This cloud had a more homogeneous structure with a ~~CDNC~~ LWC in the range between ~~60~~0.1 ~~cm~~g m^{-3} and ~~1200~~.2 ~~cm^{-3}. The mean cloud droplet diameter steadily increased from 10~~g ~~m to 16~~ m^{-3}. A low-level cloud was also observed by the cloud base observations of the ceilometer located in Klosters (not shown).

The interesting observation was that the low-level cloud dissipated during P2_unbl, when the low-level flow turned from a blocked to an unblocked state, pointing to the importance of the blocking situation in forming and sustaining the low-level liquid cloud. We suggest that an overturning cell formed as a consequence of the low-level flow impinging on the mountain barrier B2 located downstream of Wolfgang (as shown in Fig. 14a), which generated an in-valley circulation with a low-level

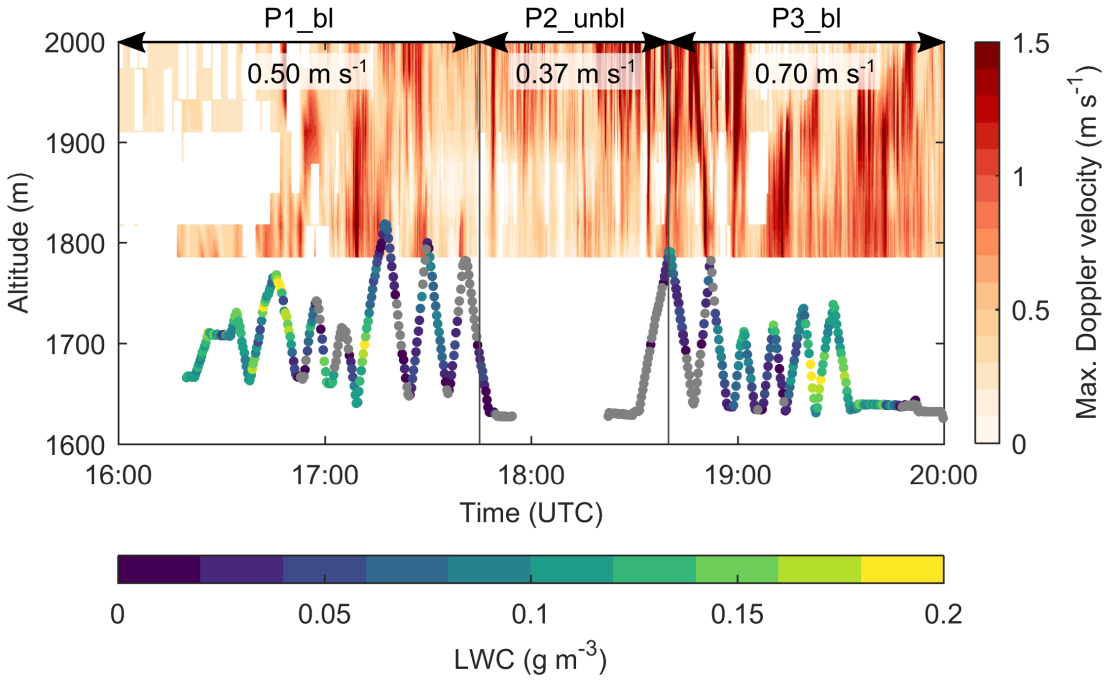

Figure 12. Vertical profiles of the ~~CDNC (a) and mean droplet diameter (b)~~ liquid water content measured with the HoloBalloon platform. ~~The lidar attenuated backscatter coefficient in the lowest levels is shown in the background.~~ Data points with a liquid water content below 0.01 g m^{-3} are indicated by gray dots. No measurements were obtained between 17:50 UTC and 18:20 UTC. The maximum Doppler velocity, which was derived from the Doppler spectra and was used as a proxy for the updraft velocity, is shown by the colorfill. The values at the top indicate the mean maximum Doppler velocity for the periods P1_bl, P2_unbl and P3_bl averaged over the height interval between the surface and 1850 m.

counterflow from Klosters towards Davos. Several weather stations ~~near Davos~~ in the Davos region confirm that a counterflow was present during P1_bl and P3_bl (Fig. 6). Since Wolfgang is located on a small-scale topographic feature (400 m), the low-level flow was forced to rise from Klosters (1200 m) to Wolfgang (1630 m) over the local topography and thereby acted as an updraft source, which led to the formation of a low-level feeder cloud. Indeed, the cloud radar indicated the presence of ~~updrafts below 2000~~higher Doppler velocities and thus higher updraft velocities during P1_bl (0.5 ~~m (i.e., positive Doppler velocities) after 19~~m ~~UTC~~ s^{-1}) and P3_bl (0.7 m s^{-1}) (Fig. ~~3b~~12). When the blocking weakened and the updraft velocity decreased during P2_unbl (0.37 m s^{-1}), the low-level cloud at Wolfgang dissipated ~~because of the missing~~ likely due to insufficient upward motion to sustain the production of liquid water. ~~This observation points~~ The correlation plots between different dynamical (mean and maximum Doppler velocity) and microphysical properties (LWC, CDNC, mean diameter) in Figure 13 further support the assumption that the updrafts driven by the in-valley circulation induced the formation of the low-level liquid cloud. Moderate positive Spearman's rank correlation coefficients were observed between the maximum Doppler velocity (v_{max}) and

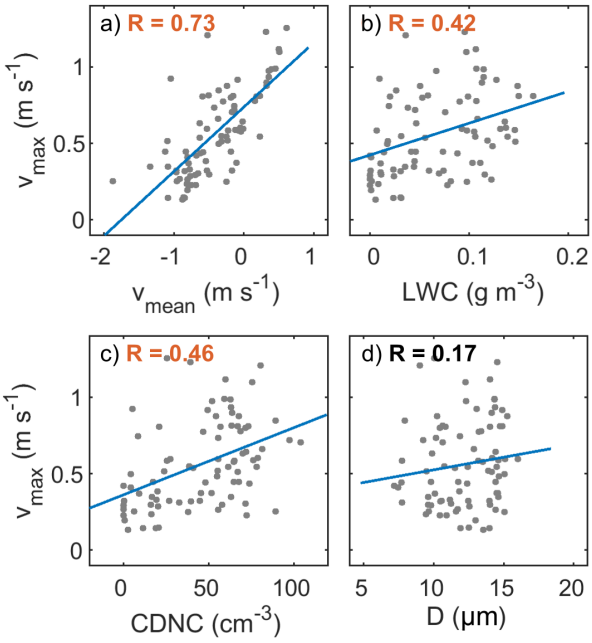

Figure 13. Correlations among dynamical (v_{mean}, v_{max}) and microphysical parameters (LWC, CDNC, D) of the low-level cloud properties. The dynamical properties that were observed with the cloud radar were averaged between the surface and 1850 m. The gray dots represent the 2-minute averages for the time periods between 16:20 UTC - 17:55 UTC and 18:30 UTC - 19:45 UTC. The blue lines indicate the least square regression line. The Spearman's rank correlation coefficient are shown at the top left corner, where correlation coefficients highlighted in orange indicate correlations significantly different from zero (5% significance level).

the LWC (0.42) and CDNC (0.46), whereas a weak correlation was found between the maximum Doppler velocity and the mean diameter *D* (0.17). Similar correlation coefficients were observed between the mean Doppler velocity and the microphysical properties (not shown). The increase in CDNC with increasing updraft velocity (Fig. 13c) suggests that droplet formation was limited by the vertical velocity that generates supersaturation, i.e. velocity-limited conditions were encountered at Wolfgang. This aspect is dealt with in more detail in a paper by Georgakaki et al. (2020), where they investigated the drivers of droplet formation in mixed-phase clouds using observations from the RACLETS campaign.

The results presented above point to the importance of localized flow effects that interact with the topography in producing low-level feeder clouds over small-scale topographic features. Feeder clouds can enhance orographic precipitation through the seeder-feeder mechanism (Bergeron, 1965; Bader and Roach, 1977; Hill et al., 1981), by providing an environment where hydrometeors that formed aloft (i.e., in the seeder region) can "feed" on the low-level liquid layer and enhance precipitation by riming and depositional growth. The seeder-feeder mechanism was for example visible in the cloud radar observations between 19 UTC and 20 UTC (Fig. 3a). ~~In~~ We assume that in the present case study ~~, this~~ the low-level feeder cloud did not play a crucial role for precipitation enhancement, as a significant fraction of the hydrometeor mass sublimated before reaching the feeder

cloud~~and precipitation was highest when the flow was unblocked~~. However, ~~we~~ in other cases of the RACLETS campaign, we found that orographically-induced low-level feeder clouds could enhance precipitation through the seeder-feeder mechanism and provide an environment for secondary ice production mechanisms (Ramelli et al., 2020b). We propose that local flow effects such as low-level blocking can also induce the formation of feeder clouds in other mountain valleys and in hilly regions and suggest that the extent of this effect depends on the strength of the blocking, the thermodynamics of the atmosphere and the altitude of the small-scale topographic feature that is located upstream of the mountain barrier.

5 Discussion

The microphysical evolution of the mixed-phase cloud and the low-level feeder cloud in the inner-Alpine valley ~~was~~ were determined by a complex interplay between orography, dynamics and microphysics. A conceptual overview of the observed ~~cloud~~ clouds is shown in Figure 14 (a: blocked state; b: unblocked state). Primary ice nucleation was suggested to occur close to the cloud top in the embedded supercooled liquid cloud layer. Based on the cloud top temperature and cloud radar and hydrometeor observations, dendrites and hexagonal plates were assumed to form, which could rapidly grow by vapor deposition. The ice particles encountered a turbulent shear layer while falling through the cloud, within which changes in the microphysical cloud properties were observed including enhanced radar reflectivity (i.e., increased ice growth) and LDR (i.e., change in particle shape or density). This suggests that the turbulent shear layer created an ice supersaturated environment and thereby influenced the cloud microphysics.

Previous studies identified flow blocking and shear-induced turbulence as a microphysical pathway for enhancing snow growth and precipitation (e.g., Marwitz, 1983; Overland and Bond, 1995; Yu and Smull, 2000; Hogan et al., 2002; Neiman et al., 2002; Neiman et al., 2004; Houze Jr and Medina, 2005; Loescher et al., 2006; Olson et al., 2007; Olson and Colle, 2009; Geerts et al., 2011; Medina and Houze Jr, 2015; Grazioli et al., 2015; Aikins et al., 2016). Different microphysical processes have been proposed to occur in ~~the turbulent layer~~turbulent layers, such as enhanced growth by riming due to pockets of higher liquid water content (e.g., Houze Jr and Medina, 2005; Medina and Houze Jr, 2015 Grazioli et al., 2015) or enhanced growth by aggregation due to increased collisions between hydrometeors (e.g., Geerts et al., 2011; Aikins et al., 2016). Based on the cloud radar observations and the ground-based snow particle measurements, we suggest that ~~depositional growth~~ riming and aggregation were the dominant ice growth mechanisms in the present case study. ~~Riming~~ The increase in the LDR at the upper edge of the shear layer was assumed to ~~play only a minor role,~~ be related to riming, as the LDR of the faster falling part of the spectrum was increased likely due to the ~~low LWP (< 100 g m^{-2}) observed by the microwave radiometer (Fig. 4c). Furthermore, the hydrometeors observed at the surface appeared primarily unrimed and indicated the presence of aggregates, dendrites and irregular ice particles (Fig. 11~~higher particle density (Fig. 10b). Depending on the rime mass fraction, riming can have a significant impact on the ice particle properties (Li et al., 2018; Moisseev et al., 2017).

~~Furthermore, an increase in the LDR (>-25 dB; i.e., column-like ice particles) was observed~~ In addition, secondary ice production processes might have been active within the shear layer~~(Fig. 10b and Fig. 3d), which is indicative for a change in the hydrometeor shape. Based on the prevailing temperature near cloud base~~. The prevailing temperature (from -8 °C to -5 °C) ~~and~~

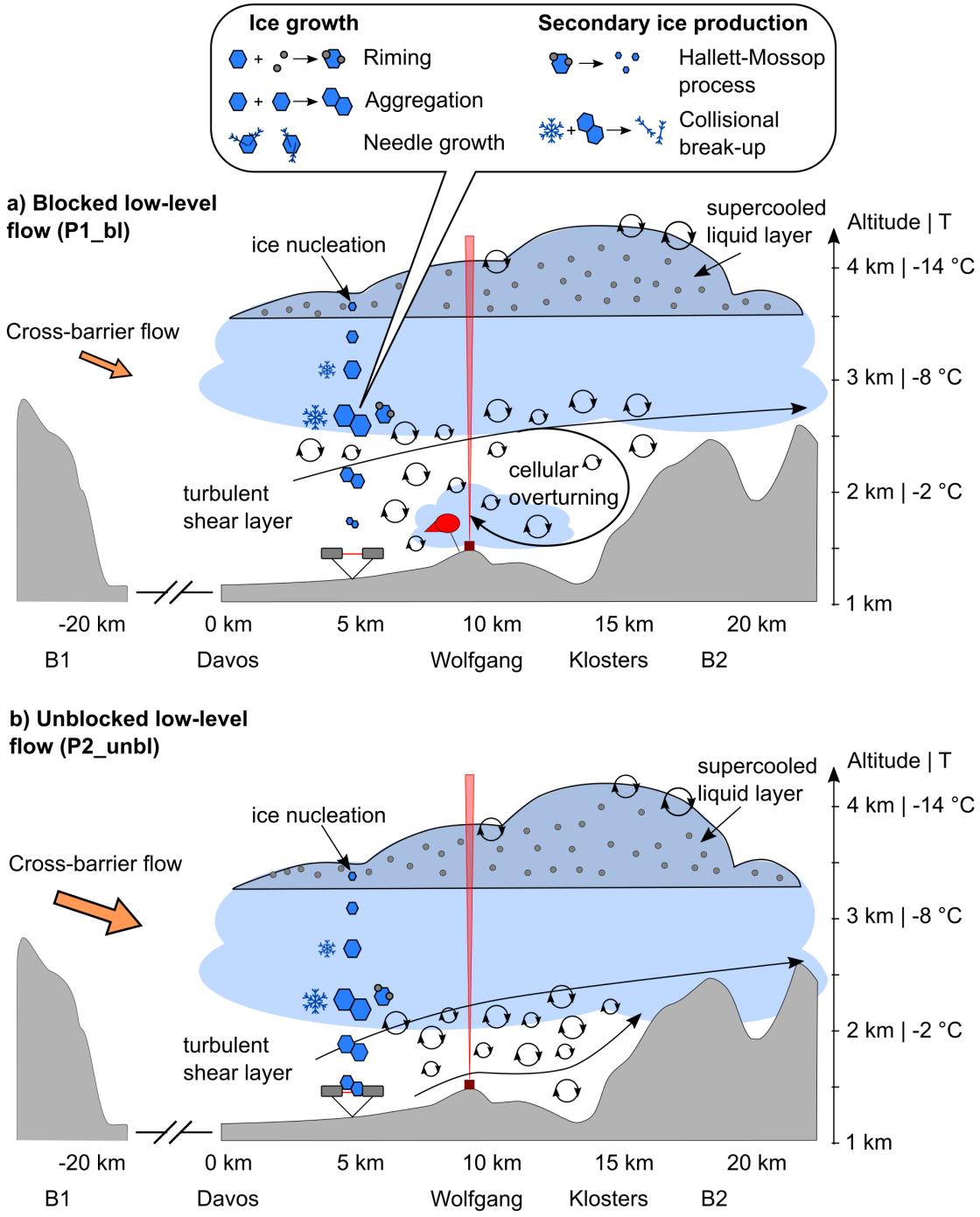

Figure 14. Conceptual overview of the dynamical and microphysical processes observed ~~in~~ within the mid-level cloud and low-level feeder cloud during ~~a~~ low-level blocked flow (a) and unblocked flow (b) (see text for more details).

the ice particle habits observed at the surface (Fig. 11), we was in the range of the Hallett-Mossop process. Furthermore, the ice particles observed near the surface suggest that needle growth occurred on the existing ice particles within the turbulent shear layer . (Fig. 11). Previous laboratory studies have observed needle growth at temperatures of -5 °C slightly below liquid water saturation (Knight, 2012). Thus, if If fragile ice crystals such as dendrites or ice particles with needle-like structures collide with large ice rimed particles, small ice fragments can might break off and lead to the production of secondary ice particles (e.g. Vardiman, 1978; Yano et al., 2016). Previous studies have observed a large number of small ice particles within turbulent shear layers, which were likely generated through secondary ice production mechanisms (e.g., Hogan et al., 2002; Grazioli et al., 2015). For example, Hogan et al. (2002) observed high concentrations of small ice particles (100 - 1000 L^{-1}) in and above a region of embedded convection, which were likely produced through the Hallett-Mossop mechanism during riming. Since the fall velocity of small ice particles is low, these secondary ice particles were found to recirculate in the updrafts /turbulent region and to feed the regions above the shear layer with ice crystals (Hogan et al., 2002; Grazioli et al., 2015), where they could continue growing to precipitation-sized particles and act as a seed to trigger secondary ice production. The Hallett-Mossop process was likely not occurring in the present case study due to the lack of supercooled liquid water in the turbulent shear layer. Rather collisional ice multiplication of fragile ice crystals (i.e., needles, dendrites) may have been responsible for the increase in the LDR and in the radar reflectivity within the turbulent shear layer. Additionally, a few laboratory-based studies suggested that ice fragmentation upon sublimation can lead to the production of secondary ice particles (e.g., Oraltay and Hallett, 1989; Dong et al., 1994; Bacon et al., 1998). However, secondary ice particles that formed within a subsaturated environment need to be transported to an ice supersaturated environment to influence the cloud microphysics (Korolev et al., 2020). In order to further investigate the role of secondary ice production in the turbulent shear layer, in situ observations of the cloud properties would be useful. Unfortunately, the tethered balloon system was limited to lower altitudes and could not sample the cloud properties within the upper part of the shear layer.

While previous research that investigated orographic precipitation has mainly focused on a single mountain barrierisolated mountain barriers, here we studied the role of low-level blocking and shear-induced turbulence on the microphysics of a mixed-phase cloud cloud microphysics in a more complex terrain with narrow valleys and a series of mountain barriers. We found that the height of the shear layerand the cloud base , the onset of the sublimation layer and as a consequence the amount of precipitation in the valley were determined by the strength of the downward propagating cross-barrier flow and on the upstream mountain barrier B1 and the strength of the low-level blocking . on the windward slope of the downstream mountain barrier B2 (Sect. 4.2). Furthermore, we found that local flow effects in mountain valleys (i.e., overturning cell in-valley circulation due to blocked low-level flow) can induce the formation of low-level feeder clouds , which can by producing local updrafts and thus enhance orographic precipitation through the seeder-feeder mechanism . Thus, this (Sect. 4.3). This case study demonstrates that it can be is challenging to study 'simple' conceptual mechanisms in complex terrain , due to numerous interactions between dynamics, microphysics and orography on different scales and the superposition of upstream and downstream effects. Nevertheless, it is important to perform field campaigns in complex terrain in order to improve our understanding of these processes and of orographic precipitation. Field campaigns in complex terrain should be designed in such a way that an extensive set of complementary instruments are deployed over the measurement area. The present observations were obtained in a region of

10 km × 10 km and mostly focused on the vertical structure. Information about the horizontal cloud structure (e.g., radar RHI scans, in situ aircraft observations) and observations over a larger area (e.g., covering the entire region between upstream and downstream mountain barriers) would be beneficial to obtain a more complete picture of the cloud dynamics and microphysics.

6 Conclusions

In this paper, we studied the influence of low-level flow blocking and shear-induced turbulence on the microphysics of a ~~mixed-phase cloud in an inner-Alpine valley~~mid-level cloud in a post-frontal environment and a low-level feeder cloud induced by an in-valley circulation. Observations from a multi-dimensional set of ground-based remote sensing, balloon-borne in situ and ground-based precipitation instruments were analyzed, which were acquired during the RACLETS campaign in the Swiss Alps. The key findings are summarized as follows:

- The ~~dynamical and microphysical structure of a mid-level cloud was characterized using ground-based remote sensing instrumentation (e.g., Ka-band polarimetric cloud radar, Raman lidar, radar wind profiler). The wind profiler~~ wind observations indicated the transition from a blocked to an unblocked low-level flow during the observational period and the presence of a ~~shear-induced turbulent~~ shear layer, which separated the blocked layer in the valley from the stronger cross-barrier flow aloft. A supercooled liquid layer was embedded near cloud top, which provided a favorable environment for ice nucleation and growth. Changes in the microphysical cloud properties were observed within the turbulent shear layer including enhanced LDRs (i.e., change in particle shape or density) and increased radar reflectivities (i.e., enhanced ice growth). Our results are consistent with previous studies that have observed enhanced ice growth and precipitation formation through riming and aggregation in turbulent layers. In addition, based on the ~~enhanced LDR and the~~ ice particle habits observed at the surface, we suggest that needle growth on existing ice particles occurred within the turbulent layer and that collisions of these fragile ice crystals ~~(e.g., dendrites, needle-like structures) with large~~ with large rimed ice particles might have caused mechanical break-up and the subsequent production of small secondary ice particles. These ice fragments have the potential to recirculate in the shear layer and influence the cloud microphysics aloft. However, this process could not be directly measured in this study. Further studies are required to investigate the role of secondary ice production mechanisms in turbulent shear layers.

- The altitude of the shear layer was determined by a complex interplay of upstream and downstream effects. For example, the shear layer was observed to lower as stronger cross-barrier flow ~~moved over the upstream mountain barrier~~ propagated downward and the low-level blocking weakened ~~. The cloud base~~ on the windward slope of the downstream mountain barrier. The beginning of the sublimation layer was found to be associated with the shear layer. Precipitation was only observed in the valley when the shear layer was at its lowest altitude. The resulting lower ~~cloud base altitude~~ sublimation layer reduced the time that the ice particles spent in the subsaturated environment, ultimately allowing for the precipitation to reach the surface. Thus, we propose that the amount of precipitation observed in a mountain valley is influenced by several factors such as (1) the strength of the cross-barrier flow and low-level blocking, (2) the vertical position of the turbulent shear layer and ~~cloud base and~~ (3) the thermodynamic state of the boundary layer.

– In situ instrumentation on a tethered balloon system observed a low-level feeder cloud, which dissipated when the low-level flow turned from a blocked to an unblocked state. We ~~suggest~~ propose that an overturning cell formed as a consequence of the low-level flow impinging on the downstream mountain barrier, which created an in-valley circulation. As a small-scale topographic feature was located upstream of the mountain barrier, we suggest that the generated counterflow (i.e., blocked flow) was forced to rise over the local topography and thereby acted as an updraft source and as a driving force for the formation of a low-level feeder cloud. Although we assume that the feeder cloud did not enhance precipitation in the present case (due to the dry boundary layer aloft), we propose that local flow effect such as low-level blocking can induce the formation of feeder clouds in other mountain valleys or on the leeward slope of foothills upstream of the main mountain barrier, where they can enhance orographic precipitation through the seeder-feeder mechanism.

Appendix A: Froude number

The dynamical response of a stable flow encountering a mountain barrier depends on the strength of the upstream airflow, the thermodynamic stability of the flow and the height of the mountain barrier. These components can be combined into a dimensionless number (Froude number; e.g., Colle et al., 2013):

$$Fr = \frac{U}{hN} \tag{A1}$$

where U is the wind speed perpendicular to the mountain barrier, h is the height of the mountain barrier and N is the Brunt-Väisälä frequency, which is a measure for the atmospheric stability. If the Froude number is large (~~Fr~~$Fr \gg 1$), the air flow can rise over the mountain barrier. When the Froude number is small (~~Fr~~$Fr \ll 1$), the upstream flow is blocked and cannot ascend over the mountain barrier. The parameters to calculate the Froude number for the periods P1_bl (16 - 17:45 UTC), P2_unbl (17:45 - 18:40 UTC) and P3_bl (18:40 - 20 UTC) are given in Table A1.

The effective terrain height h ~~between the valley and the mountain barrier (2700 m)~~ was around 800 m (see ~~B2 in~~ Fig. 1b). The wind speed was obtained from the radar wind profiler and averaged over the ~~1600~~2100 - 2800 m height interval. The temperature and pressure were measured at Wolfgang (1630 m) and at Weissfluhjoch (2700 m) and a linear temperature gradient was assumed between the two measurement locations. The calculated Froude numbers were below 1 for all periods, indicative for a blocked low-level flow. The Froude number increased during P2_unbl (from 0.75 to 0.94), suggesting a weakening of the blocking.

Appendix B: ~~Correlation between dynamics, microphysics and precipitation~~

~~To quantify the interactions between dynamics, microphysics and precipitation, correlation coefficients were calculated between the different parameters of Figure 9 (see Table **??**). Correlation between (1) the height of the 10 m s^{-1} km^{-1} wind shear contour line, (2) the height of maximum radar reflectivity and (3) the precipitation rate measured at Wolfgang. The Spearman's rank correlation coefficient ρ and their p-Values are shown. The correlation coefficients were calculated between 16:45 UTC and 18:30 UTC. A time lag of 10 min was applied to the precipitation measurements.~~ ~~Height shear layer Height max. reflectivity~~

Table A1. Parameters used to calculate the Froude number during P1_bl, P2_unbl and P3_bl.

	Wolfgang		Weissfluhjoch				
	T (°C)	p (hPa)	T (°C)	p (hPa)	U ($m\,s^{-1}$)	N (s^{-1})	Froude number
P1_bl	0.1	827.7	-5.2	725.6	7.6	0.013	0.75
P2_unbl	-0.1	828.4	-5.6	726.4	9.3	0.012	0.94
P3_bl	-0.2	829.2	-5.9	726.8	6.7	0.012	0.69

~~Precipitation rateHeight shear layer - 0.62 (< 0.001) -0.76 (< 0.001)Height max. reflectivity 0.62 (< 0.001) - -0.55 (< 0.001)Precipitation rate -0.76 (< 0.001) -0.55 (< 0.001) -A moderate positive Spearman's rank correlation (ρ = 0.62) was observed between the shear layer height and the altitude of maximum radar reflectivity. On the other hand, a negative correlation was found between the precipitation rate and the shear layer height (ρ = -0.76) and altitude of maximum radar reflectivity (ρ = -0.55). All correlations were significant at the 5% confidence level. The moderate to strong correlations between dynamics, microphysics and precipitation parameters suggest that interactions between dynamical and microphysical processes were active within the turbulent shear layer, which enhanced ice growth and precipitation formation.~~

Code and data availability. The dataset of this study is available for download at: https://doi.org/10.5281/zenodo.4338815 (Ramelli et al., 2020c). The scripts to reproduce the figures of this study are available at: https://doi.org/10.5281/zenodo.4339254 (Ramelli et al., 2020d). The elevation data was obtained from the digital height model DHM25 of the Federal Office of Topography swisstopo: https://shop.swisstopo.admin.ch/de/products/height_models/dhm25200 (last access: 9 March 2020). The ERA5 reanalysis data can be accessed from the Copernicus Climate Change Service (C3S): https://doi.org/10.24381/cds.bd0915c6 (Hersbach et al., 2018; last access: 18 December 2020). The radiosonde data was acquired from the UQAM-Montreal Weather Centre: http://meteocentre.com/radiosonde/ (access: 16 March 2020). The datasets of the RACLETS campaign are available for download at: https://www.envidat.ch/group/raclets-field-campaign (last access: 18 December 2020).

Author contributions. FR analyzed the observational data and prepared the figures of the manuscript. FR, JH, JP, AL and JW performed the HoloBalloon measurements. JB and PS processed the remote sensing data and helped in interpreting the remote sensing observations. RE operated the OCEANET container during the RACLETS campaign. MH operated the radar wind profiler and processed the wind profiler data. FR, JH, RD and UL helped in analyzing and interpreting the data. FR prepared the manuscript with contributions from all authors.

Competing interests. The authors declare that they have no conflict of interest

Acknowledgements. The authors would like to thank the participants of the RACLETS campaign for their technical support and many fruitful discussions. In particular, we are thankful to Michael Lehning (WSL/SLF, EPFL) and his whole team for their substantial support for realizing the RACLETS campaign by providing local contacts and support in requesting the necessary permissions. We would like to thank Paul Fopp for providing his land for the RACLETS campaign. We would also like to thank Alexander Beck for helping with the organization of the field campaign. Moreover, the authors are thankful to Susanne Crewell (University of Cologne) and Bernhard Pospichal (University of Cologne) for their help in interpreting the microwave radiometer data. We would also like to acknowledge Benjamin Walter (SLF) for providing data of the snowdrift station located at Gotschnagrat. We thank the Swiss Federal Office of Meteorology and Climatology ~~MeteoSwiss~~ for providing the meteorological measurements, ceilometer data from Klosters, MASC observations and access to the COSMO1 and weather radar data. Furthermore, we would also like to thank Eberhard Bodenschatz (MPI Goettingen) for his technical support during the development of the HoloBalloon platform. We would like to thank the Federal Office of Civil Aviation, particularly Judith Baumann and Jeroen Kroese, for their pragmatic approach in obtaining the flight permit. ~~FR, JH, AL, JP, JW and UL acknowledge funding from the Swiss National Science Foundation (SNSF) grant number 200021_175824. RD would like to acknowledge funding from the European Research Council (ERC) through Grant StG 758005.~~ Finally, we thank Dmitri Moisseev and an anonymous reviewer for their constructive and helpful feedback on the manuscript, which strengthened the paper.

Financial support. This research has been supported by the Swiss National Science Foundation (SNSF) grant number 200021_175824. Robert O. David would like to acknowledge funding from the European Research Council (ERC) through Grant StG 758005.

Review statement. This paper was edited by Ari Laaksonen and reviewed by Dmitri Moisseev and an anonymous referee.

References

Aikins, J., Friedrich, K., Geerts, B., and Pokharel, B.: Role of a cross-barrier jet and turbulence on winter orographic snowfall, Monthly Weather Review, 144, 3277–3300, 2016.

Bacon, N. J., Swanson, B. D., Baker, M. B., and Davis, E. J.: Breakup of levitated frost particles, Journal of Geophysical Research: Atmospheres, 103, 13 763–13 775, 1998.

Bader, M. and Roach, W.: Orographic rainfall in warm sectors of depressions, Quarterly Journal of the Royal Meteorological Society, 103, 269–280, 1977.

Bailey, M. P. and Hallett, J.: A comprehensive habit diagram for atmospheric ice crystals: Confirmation from the laboratory, AIRS II, and other field studies, Journal of the Atmospheric Sciences, 66, 2888–2899, 2009.

Beck, A., Henneberger, J., Schöpfer, S., Fugal, J., and Lohmann, U.: HoloGondel: in situ cloud observations on a cable car in the Swiss Alps using a holographic imager, Atmospheric Measurement Techniques, 10, 459–476, 2017.

Bergeron, T.: On the low-level redistribution of atmospheric water caused by orography, in: Suppl. Proc. Int. Conf. Cloud Phys., Tokyo, 1965, pp. 96–100, 1965.

Borys, R. D., Lowenthal, D. H., Cohn, S. A., and Brown, W. O.: Mountaintop and radar measurements of anthropogenic aerosol effects on snow growth and snowfall rate, Geophysical Research Letters, 30, 2003.

Bringi, V. N. and Chandrasekar, V.: Polarimetric Doppler weather radar: principles and applications, Cambridge university press, 2001.

Bühl, J., Seifert, P., Myagkov, A., and Ansmann, A.: Measuring ice-and liquid-water properties in mixed-phase cloud layers at the Leipzig Cloudnet station, 2016.

Chapman, D. and Browning, K.: Measurements of dissipation rate in frontal zones, Quarterly Journal of the Royal Meteorological Society, 127, 1939–1959, 2001.

Colle, B. A., Smith, R. B., and Wesley, D. A.: Theory, observations, and predictions of orographic precipitation, in: Mountain Weather Research and Forecasting, pp. 291–344, Springer, 2013.

Dong, Y., Oraltay, R. G., and Hallett, J.: Ice particle generation during evaporation, Atmospheric research, 32, 45–53, 1994.

Durran, D. R.: Mountain waves and downslope winds, in: Atmospheric processes over complex terrain, pp. 59–81, Springer, 1990.

Engelmann, R., Kanitz, T., Baars, H., Heese, B., Althausen, D., Skupin, A., Wandinger, U., Komppula, M., Stachlewska, I. S., Amiridis, V., et al.: The automated multiwavelength Raman polarization and water-vapor lidar PollyXT: the neXT generation, Atmospheric Measurement Techniques, 9, 1767–1784, 2016.

Frei, C. and Schär, C.: A precipitation climatology of the Alps from high-resolution rain-gauge observations, International Journal of Climatology: A Journal of the Royal Meteorological Society, 18, 873–900, 1998.

Garrett, T., Fallgatter, C., Shkurko, K., and Howlett, D.: Fall speed measurement and high-resolution multi-angle photography of hydrometeors in free fall, Atmospheric Measurement Techniques, 5, 2625–2633, 2012.

Geerts, B., Miao, Q., and Yang, Y.: Boundary layer turbulence and orographic precipitation growth in cold clouds: Evidence from profiling airborne radar data, Journal of the atmospheric sciences, 68, 2344–2365, 2011.

Georgakaki, P., Bougiatioti, A., Wieder, J., Mignani, C., Ramelli, F., Kanji, Z. A., Henneberger, J., Hervo, M., Berne, A., Lohmann, U., et al.: On the drivers of droplet variability in Alpine mixed-phase clouds, Atmospheric Chemistry and Physics Discussions, pp. 1–35, 2020.

Görsdorf, U., Lehmann, V., Bauer-Pfundstein, M., Peters, G., Vavriv, D., Vinogradov, V., and Volkov, V.: A 35-GHz polarimetric Doppler radar for long-term observations of cloud parameters—Description of system and data processing, Journal of Atmospheric and Oceanic Technology, 32, 675–690, 2015.

Grazioli, J., Lloyd, G., Panziera, L., Hoyle, C. R., Connolly, P. J., Henneberger, J., and Berne, A.: Polarimetric radar and in situ observations of riming and snowfall microphysics during CLACE 2014, Atmospheric Chemistry and Physics, 15, 13 787–13 802, 2015.

Hallett, J. and Mossop, S.: Production of secondary ice particles during the riming process, Nature, 249, 26, 1974.

Henneberger, J., Fugal, J., Stetzer, O., and Lohmann, U.: HOLIMO II: a digital holographic instrument for ground-based in situ observations of microphysical properties of mixed-phase clouds, Atmospheric Measurement Techniques, 6, 2975–2987, 2013.

Hersbach, H., Bell, B., Berrisford, P., Biavati, G., Horányi, A., Muñoz Sabater, J., Nicolas, J., Peubey, C., Radu, R., Rozum, I., Schepers, D., Simmons, A., Soci, C., Dee, D., and Thépaut, J.-N.: ERA5 hourly data on single levels from 1979 to present, Copernicus Climate Change Service (C3S) Climate Data Store (CDS), https://doi.org/10.24381/cds.adbb2d47, 2018.

Hill, F., Browning, K., and Bader, M.: Radar and raingauge observations of orographic rain over south Wales, Quarterly Journal of the Royal Meteorological Society, 107, 643–670, 1981.

Hogan, R. J., Field, P., Illingworth, A., Cotton, R., and Choularton, T.: Properties of embedded convection in warm-frontal mixed-phase cloud from aircraft and polarimetric radar, Quarterly Journal of the Royal Meteorological Society: A journal of the atmospheric sciences, applied meteorology and physical oceanography, 128, 451–476, 2002.

Houze Jr, R. A.: Orographic effects on precipitating clouds, Reviews of Geophysics, 50, 2012.

Houze Jr, R. A.: Cloud dynamics, Academic press, 2014.

Houze Jr, R. A. and Medina, S.: Turbulence as a mechanism for orographic precipitation enhancement, Journal of the atmospheric sciences, 62, 3599–3623, 2005.

Jiang, Q. and Smith, R. B.: Cloud timescales and orographic precipitation, Journal of the atmospheric sciences, 60, 1543–1559, 2003.

Keyser, D. and Shapiro, M.: A review of the structure and dynamics of upper-level frontal zones, Monthly Weather Review, 114, 452–499, 1986.

Kirshbaum, D. J., Adler, B., Kalthoff, N., Barthlott, C., and Serafin, S.: Moist orographic convection: Physical mechanisms and links to surface-exchange processes, Atmosphere, 9, 80, 2018.

Kneifel, S. and Moisseev, D.: Long-Term Statistics of Riming in Nonconvective Clouds Derived from Ground-Based Doppler Cloud Radar Observations, Journal of the Atmospheric Sciences, 77, 3495–3508, 2020.

Knight, C. A.: Ice growth from the vapor at- 5° C, Journal of the atmospheric sciences, 69, 2031–2040, 2012.

Korolev, A., Heckman, I., Wolde, M., Ackerman, A. S., Fridlind, A. M., Ladino, L. A., Lawson, R. P., Milbrandt, J., and Williams, E.: A new look at the environmental conditions favorable to secondary ice production, Atmospheric Chemistry and Physics, 20, 1391–1429, https://doi.org/10.5194/acp-20-1391-2020, https://www.atmos-chem-phys.net/20/1391/2020/, 2020.

Lauber, A., Henneberger, J., Mignani, C., Ramelli, F., Pasquier, J. T., Wieder, J., Hervo, M., and Lohmann, U.: Continuous secondary ice production initiated by updrafts through the melting layer in mountainous regions, Atmospheric Chemistry and Physics Discussions, pp. 1–26, 2020.

Li, H., Moisseev, D., and von Lerber, A.: How does riming affect dual-polarization radar observations and snowflake shape?, Journal of Geophysical Research: Atmospheres, 123, 6070–6081, 2018.

Loescher, K. A., Young, G. S., Colle, B. A., and Winstead, N. S.: Climatology of barrier jets along the Alaskan coast. Part I: Spatial and temporal distributions, Monthly weather review, 134, 437–453, 2006.

Lohmann, U., Lüönd, F., and Mahrt, F.: An introduction to clouds: From the microscale to climate, Cambridge University Press, 2016.

Löhnert, U., Schween, J., Acquistapace, C., Ebell, K., Maahn, M., Barrera-Verdejo, M., Hirsikko, A., Bohn, B., Knaps, A., O'connor, E., et al.: JOYCE: Jülich observatory for cloud evolution, Bulletin of the American Meteorological Society, 96, 1157–1174, 2015.

Lowenthal, D. H., Borys, R. D., Cotton, W., Saleeby, S., Cohn, S. A., and Brown, W. O.: The altitude of snow growth by riming and vapor deposition in mixed-phase orographic clouds, Atmospheric environment, 45, 519–522, 2011.

Magono, C. and Lee, C. W.: Meteorological classification of natural snow crystals, Journal of the Faculty of Science, Hokkaido University. Series 7, Geophysics, 2, 321–335, 1966.

Marwitz, J. D.: The kinematics of orographic airflow during Sierra storms, Journal of the atmospheric sciences, 40, 1218–1227, 1983.

Medina, S. and Houze, R. A.: Air motions and precipitation growth in Alpine storms, Quarterly Journal of the Royal Meteorological Society: A journal of the atmospheric sciences, applied meteorology and physical oceanography, 129, 345–371, 2003.

Medina, S. and Houze Jr, R. A.: Small-scale precipitation elements in midlatitude cyclones crossing the California Sierra Nevada, Monthly Weather Review, 143, 2842–2870, 2015.

Medina, S., Smull, B. F., Houze Jr, R. A., and Steiner, M.: Cross-barrier flow during orographic precipitation events: Results from MAP and IMPROVE, Journal of the atmospheric sciences, 62, 3580–3598, 2005.

Medina, S., Sukovich, E., and Houze Jr, R. A.: Vertical structures of precipitation in cyclones crossing the Oregon Cascades, Monthly weather review, 135, 3565–3586, 2007.

Melchionna, S., Bauer, M., and Peters, G.: A new algorithm for the extraction of cloud parameters using multipeak analysis of cloud radar data–first application and preliminary results, Meteorologische Zeitschrift, 17, 613–620, 2008.

Mignani, C., Wieder, J., Sprenger, M. A., Kanji, Z. A., Henneberger, J., Alewell, C., and Conen, F.: Towards parametrising atmospheric concentrations of ice nucleating particles active at moderate supercooling, Atmospheric Chemistry and Physics Discussions, pp. 1–7, 2020.

Moisseev, D., von Lerber, A., and Tiira, J.: Quantifying the effect of riming on snowfall using ground-based observations, Journal of Geophysical Research: Atmospheres, 122, 4019–4037, 2017.

Mosimann, L.: An improved method for determining the degree of snow crystal riming by vertical Doppler radar, Atmospheric research, 37, 305–323, 1995.

Myagkov, A., Seifert, P., Wandinger, U., Bühl, J., and Engelmann, R.: Relationship between temperature and apparent shape of pristine ice crystals derived from polarimetric cloud radar observations during the ACCEPT campaign, 2016.

Neiman, P. J., Ralph, F. M., White, A., Kingsmill, D., and Persson, P.: The statistical relationship between upslope flow and rainfall in California's coastal mountains: Observations during CALJET, Monthly Weather Review, 130, 1468–1492, 2002.

Neiman, P. J., Martin Ralph, F., Persson, P. O. G., White, A. B., Jorgensen, D. P., and Kingsmill, D. E.: Modification of fronts and precipitation by coastal blocking during an intense landfalling winter storm in southern California: Observations during CALJET, Monthly weather review, 132, 242–273, 2004.

North, G. R., Pyle, J. A., and Zhang, F.: Encyclopedia of atmospheric sciences, vol. 1, Elsevier, 2014.

Olson, J. B. and Colle, B. A.: Three-dimensional idealized simulations of barrier jets along the southeast coast of Alaska, Monthly weather review, 137, 391–413, 2009.

Olson, J. B., Colle, B. A., Bond, N. A., and Winstead, N.: A comparison of two coastal barrier jet events along the southeast Alaskan coast during the SARJET field experiment, Monthly weather review, 135, 2973–2994, 2007.

Oraltay, R. and Hallett, J.: Evaporation and melting of ice crystals: A laboratory study, Atmospheric research, 24, 169–189, 1989.

Overland, J. E. and Bond, N. A.: Observations and scale analysis of coastal wind jets, Monthly Weather Review, 123, 2934–2941, 1995.

Pinsky, M. and Khain, A.: Some effects of cloud turbulence on water–ice and ice–ice collisions, Atmospheric research, 47, 69–86, 1998.

Pinsky, M., Khain, A., Korolev, A., and Magaritz-Ronen, L.: Theoretical investigation of mixing in warm clouds–Part 2: Homogeneous mixing, Atmospheric Chemistry and Physics, 16, 9255–9272, 2016.

Pruppacher, H. R. and Klett, J. D.: Microphysics of clouds and precipitation, Nature, 284, 88–88, 1980.

Ramelli, F., Beck, A., Henneberger, J., and Lohmann, U.: Using a holographic imager on a tethered balloon system for microphysical observations of boundary layer clouds, Atmospheric Measurement Techniques, 13, 925–939, https://doi.org/10.5194/amt-13-925-2020, https://www.atmos-meas-tech.net/13/925/2020/, 2020a.

Ramelli, F., Henneberger, J., David, R. O., Bühl, J., Radenz, M., Seifert, P., Wieder, J., Lauber, A., Pasquier, J. T., Engelmann, R., et al.: Microphysical investigation of the seeder and feeder region of an Alpine mixed-phase cloud, Atmospheric Chemistry and Physics Discussions, pp. 1–32, 2020b.

Ramelli, F., Henneberger, J., David, R. O., Lauber, A., Pasquier, J. T., Wieder, J., Bühl, J., Seifert, P., Engelmann, R., Hervo, M., and Lohmann, U.: Data for the publication "Influence of low-level blocking and turbulence on the microphysics of a mixed-phase cloud in an inner-Alpine valley", https://doi.org/10.5281/zenodo.4338816, https://doi.org/10.5281/zenodo.4338816, 2020c.

Ramelli, F., Henneberger, J., David, R. O., Lauber, A., Pasquier, J. T., Wieder, J., Bühl, J., Seifert, P., Engelmann, R., Hervo, M., and Lohmann, U.: Scripts for the publication "Influence of low- level blocking and turbulence on the microphysics of a mixed-phase cloud in an inner-Alpine valley", https://doi.org/10.5281/zenodo.4339255, https://doi.org/10.5281/zenodo.4339255, 2020d.

Rauber, R. M. and Tokay, A.: An explanation for the existence of supercooled water at the top of cold clouds, Journal of the Atmospheric Sciences, 48, 1005–1023, 1991.

Roe, G. H.: Orographic precipitation, Annu. Rev. Earth Planet. Sci., 33, 645–671, 2005.

Rose, T., Crewell, S., Löhnert, U., and Simmer, C.: A network suitable microwave radiometer for operational monitoring of the cloudy atmosphere, Atmospheric Research, 75, 183–200, 2005.

Rotunno, R. and Ferretti, R.: Mechanisms of intense Alpine rainfall, Journal of the atmospheric sciences, 58, 1732–1749, 2001.

Rotunno, R. and Houze, R. A.: Lessons on orographic precipitation from the Mesoscale Alpine Programme, Quarterly Journal of the Royal Meteorological Society: A journal of the atmospheric sciences, applied meteorology and physical oceanography, 133, 811–830, 2007.

Shupe, M. D., Kollias, P., Matrosov, S. Y., and Schneider, T. L.: Deriving mixed-phase cloud properties from Doppler radar spectra, Journal of Atmospheric and Oceanic Technology, 21, 660–670, 2004.

Shupe, M. D., Matrosov, S. Y., and Uttal, T.: Arctic mixed-phase cloud properties derived from surface-based sensors at SHEBA, Journal of the atmospheric sciences, 63, 697–711, 2006.

Smith, R. B.: The influence of mountains on the atmosphere, in: Advances in geophysics, vol. 21, pp. 87–230, Elsevier, 1979.

Smith, R. B.: 100 Years of Progress on Mountain Meteorology Research, Meteorological Monographs, 59, 20–1, 2019.

Stoelinga, M. T., Stewart, R. E., Thompson, G., and Thériault, J. M.: Microphysical processes within winter orographic cloud and precipitation systems, in: Mountain Weather Research and Forecasting, pp. 345–408, Springer, 2013.

Tokay, A., Wolff, D. B., and Petersen, W. A.: Evaluation of the new version of the laser-optical disdrometer, OTT Parsivel2, Journal of Atmospheric and Oceanic Technology, 31, 1276–1288, 2014.

Vardiman, L.: The generation of secondary ice particles in clouds by crystal–crystal collision, Journal of the Atmospheric Sciences, 35, 2168–2180, 1978.

Walter, B., Huwald, H., Gehring, J., Bühler, Y., and Lehning, M.: Radar measurements of blowing snow off a mountain ridge, The Cryosphere, 14, 1779–1794, https://doi.org/10.5194/tc-14-1779-2020, https://tc.copernicus.org/articles/14/1779/2020/, 2020.

Yano, J.-I., Phillips, V. T., and Kanawade, V.: Explosive ice multiplication by mechanical break-up in ice–ice collisions: a dynamical system-based study, Quarterly Journal of the Royal Meteorological Society, 142, 867–879, 2016.

Yu, C.-K. and Smull, B. F.: Airborne Doppler observations of a landfalling cold front upstream of steep coastal orography, Monthly Weather Review, 128, 1577–1603, 2000.

Yuter, S. E. and Houze Jr, R. A.: Three-dimensional kinematic and microphysical evolution of Florida cumulonimbus. Part II: Frequency distributions of vertical velocity, reflectivity, and differential reflectivity, Monthly weather review, 123, 1941–1963, 1995.